

PHOTONICS Research

Nonlinear optics on silicon-rich nitride—a high nonlinear figure of merit CMOS platform [Invited]

D. T. H. TAN,^{1,*} K. J. A. OOI,¹  AND D. K. T. NG²

¹Photonics Devices and Systems Group, Singapore University of Technology and Design, 8 Somapah Rd., Singapore 487372, Singapore

²Data Storage Institute, Agency for Science, Technology and Research (A*STAR), 2 Fusionopolis Way #08-01 Innovis, Singapore 138634, Singapore

*Corresponding author: dawn_tan@sutd.edu.sg

Received 24 October 2017; revised 18 January 2018; accepted 20 January 2018; posted 23 January 2018 (Doc. ID 309527); published 16 April 2018

CMOS platforms with a high nonlinear figure of merit are highly sought after for high photonic quantum efficiencies, enabling functionalities not possible from purely linear effects and ease of integration with CMOS electronics. Silicon-based platforms have been prolific amongst the suite of advanced nonlinear optical signal processes demonstrated to date. These include crystalline silicon, amorphous silicon, Hydrex glass, and stoichiometric silicon nitride. Residing between stoichiometric silicon nitride and amorphous silicon in composition, silicon-rich nitride films of various formulations have emerged recently as promising nonlinear platforms for high nonlinear figure of merit nonlinear optics. Silicon-rich nitride films are compositionally engineered to create bandgaps that are sufficiently large to eliminate two-photon absorption at telecommunications wavelengths while enabling much larger nonlinear waveguide parameters (5x–500x) than those in stoichiometric silicon nitride. This paper reviews recent developments in the field of nonlinear optics using silicon-rich nitride platforms, as well as the outlook and future opportunities in this burgeoning field. © 2018 Chinese Laser Press

OCIS codes: (190.4390) Nonlinear optics, integrated optics; (190.3270) Kerr effect.

<https://doi.org/10.1364/PRJ.6.000B50>

1. INTRODUCTION

The efficiency of nonlinear optical signal processing relies strongly on the nonlinear figure of merit and nonlinear strength of the platform. Platforms with a high nonlinear figure of merit ensure that photons involved in the nonlinear process do not get lost to nonlinear loss mechanisms such as two-photon transitions and free-carrier absorption. Nonlinear platforms that are compatible with complementary metal-oxide semiconductor (CMOS) processing are especially significant, because of their potential for low-cost manufacturing and ease of integration with the suite of electronics devices that are often needed to complement the on-chip optical system. Examples of such systems include those which have been commercialized, such as optical transceivers [1].

Among the cheapest and most prolific of CMOS materials is silicon, which possesses several unique optical properties that make it highly advantageous for integrated optics applications. Silicon possesses a bandgap of 1.1 eV, which implies optical transparency above the wavelength of 1.1 μm . The same material property that allows silicon to be an effective absorber and photodetector at the near-infrared also enables silicon to be transparent at telecommunications wavelengths, where a significant number of potential commercial applications are

located. The smaller bandgap compared to insulators yields a larger linear refractive index, which through Miller's rule also implies a stronger Kerr nonlinearity [2]. Conversely, the 1.1 eV bandgap in silicon is also insufficient to preclude two-photon transitions at telecommunications wavelengths, which, when coupled with free-carrier losses, has been shown to be detrimental to optical efficiencies at powers as low as a few hundred milliwatts [3,4].

Approaches to overcome the limitations of silicon for nonlinear optics have come about through materials grown via chemical vapor deposition. Two such materials that have seen remarkable achievements in recent times include Hydrex glass [5–9] and silicon nitride [9–15], both of which have a sufficiently wide bandgap to eliminate two-photon absorption (TPA) at telecommunications wavelengths.

Most recently, a new suite of nonlinear CMOS materials availed through chemical vapor deposition techniques has emerged. These materials may theoretically possess a continuum of refractive indices spanning from 1.46 (silica) to ~ 3.7 (amorphous silicon). Notably, the emergence of bandgap-engineered silicon-rich nitride (SRN), tailored in composition to possess a large linear refractive index without being encumbered by two-photon absorption at telecommunications

wavelengths, has become a promising new material for nonlinear optics applications. Compositionally residing between stoichiometric silicon nitride and silicon, various formulations of silicon-rich nitride films may be grown, yielding varying optical properties. This review paper covers recent progress of nonlinear optics developed on the silicon-rich nitride platform [15–29], and discusses the challenges, opportunities, and outlook for the platform.

2. GROWTH OF BANDGAP-ENGINEERED SILICON-RICH NITRIDE FILMS

Over the years, non-stoichiometric silicon nitride has been developed to provide solutions to light emission [30,31] and as an alternative to silicon for highly compact photonic light wave circuits [32–34]. The advent of silicon-rich nitride was largely enabled by the availability of chemical vapor deposition (CVD) technologies, allowing process parameters to directly tailor the optical properties of the film. Of these, inductively coupled plasma CVD (ICP-CVD) and plasma-enhanced CVD (PECVD) utilize lower temperatures (250°C and 350°C–400°C, respectively) that are well within the thermal budget for back-end CMOS processing, whereas low-pressure CVD (LPCVD) requires higher temperatures of >800°C. Nevertheless, process innovations availed by CVD techniques allow films with tailored silicon:nitrogen ratios to be designed and grown.

A. Growth Processes of Silicon-Rich Nitride Films

Stoichiometric silicon nitride films have been widely reported to be grown using PECVD or LPCVD processes [10–15,35–38]. NH_3 has been a precursor gas of choice over N_2 because the energies of N–H bonds are almost three times smaller than those of $\text{N} \equiv \text{N}$ bonds (391 kJ/mol versus 941 kJ/mol), and therefore requires less energy or temperature to break. However, the use of NH_3 gas in the deposition process has been reported to lead to unwanted N–H bonds in the deposited films [39–42]. The presence of N–H bonds in the films varies in extent depending on process conditions and contributes to absorption at telecommunications wavelengths. Consequently, avoiding the use of NH_3 as a precursor gas in the growth of silicon-rich nitride films is one approach to reduce losses at the 1.55 μm wavelength. Similar to the growth of stoichiometric silicon nitride films, silicon-rich nitride film growth has also explored use of various gas mixtures including SiH_4 with NH_3 , SiH_4 with N_2 , and dichlorosilane with NH_3 , with each combination possessing a source of silicon and nitrogen atoms. In SRN films, the mechanism for tailoring of the film composition and optical properties arises from varying the process conditions used to grow the films.

Process development using low-temperature ICP-CVD (250°C) has successfully resulted in silicon-rich nitride films with refractive indices spanning from 2.2 all the way to 3.1 (Fig. 1) [15,17]. The films with the highest refractive index ($n = 3.1$) have been characterized by X-ray photoelectron spectroscopy to possess a Si:N ratio of 7:3 and a bandgap of 2.1 eV [25]. PECVD processes (350°C) have also been successful in their ability to create silicon-rich nitride films with linear refractive indices of up to 2.7 (Figs. 2 and 3) [21,28]. In LPCVD films grown at 800°C, recent work has shown that the film

indices could be tailored from 2.0 to 2.2 [43]. When using NH_3 as a precursor gas, LPCVD films potentially allow films to have less N–H bonds compared to PECVD-grown films, because of the high growth temperatures exceeding 800°C. The drawback, however, would be the high temperature, which exceeds the back-end CMOS thermal budget. The major implication of temperature in the context of CMOS processing pertains to some of the incompatibilities of high temperatures with prior fabrication steps performed at the front end. For an optical system to be completely fabricated on the back-end process, it would require all processes to be conducted below 400°C. Particularly, if the optical system is to be integrated with electronics, processes such as copper metallization as well as doping of P–N junctions, which are performed on the front end, would be compromised through melting and dopant migration when they are subjected to high temperatures at the back end. If compatibility with back-end CMOS processing is not required, annealing of the films at temperatures of up to 1200°C could potentially be used to further eliminate any N–H present in the films and approach the limit of ultralow-loss films [44–46].

B. Optimizing Silicon-Rich Nitride Films for Nonlinear Optics

The interaction of a photon incident on a material depends very much on the material's bandgap. Optical transparency of a material at a specific wavelength requires the energy of incident photons to be smaller than the bandgap energy [47]. A larger bandgap implies tightly bound electrons, which interact minimally with an incident photon with energy below its bandgap. Materials with a larger bandgap therefore possess a smaller refractive index, and experience a shorter delay when propagating within the medium. Conversely, a photon incident in a material with a smaller bandgap will now encounter less tightly bound electrons, and photon–electron interactions will become more pronounced, generating a larger refractive index. Similarly, Miller's rule, which was formulated in the sixties to empirically describe the relationship between a large linear refractive index and second-order polarizability, also provides pertinent insight into designing for high Kerr nonlinearities through large linear refractive indices [2].

Attempts at bandgap engineering of non-stoichiometric silicon nitride have emerged for the goal of achieving maximally large nonlinear refractive indices while retaining a high nonlinear figure of merit. Drawing from Miller's rule, a streamlined method to achieve a fortuitous combination of large nonlinearity and nonlinear figure of merit [$\text{FOM}_{\text{NL}} = n_2 / (\beta_{\text{TPA}} \cdot \lambda)$, where n_2 is the nonlinear refractive index, β_{TPA} is the two-photon absorption coefficient, and λ is the wavelength] can be achieved through the maximization of the linear refractive index, with the bandgap governing onset of two-photon absorption serving as an upper bound. Amorphous silicon films with bandgap, $E_g = 1.7$ eV, which is theoretically larger than the two-photon threshold at 1.55 μm , have been shown to exhibit two-photon absorption [48–52]. This suggests that accounting for Urbach tails through a buffer in the film's bandgap is warranted. A continuum of non-stoichiometric silicon nitride materials with varying E_g values have been formulated, and silicon-rich nitride films with $E_g = 2.1$ eV have been shown

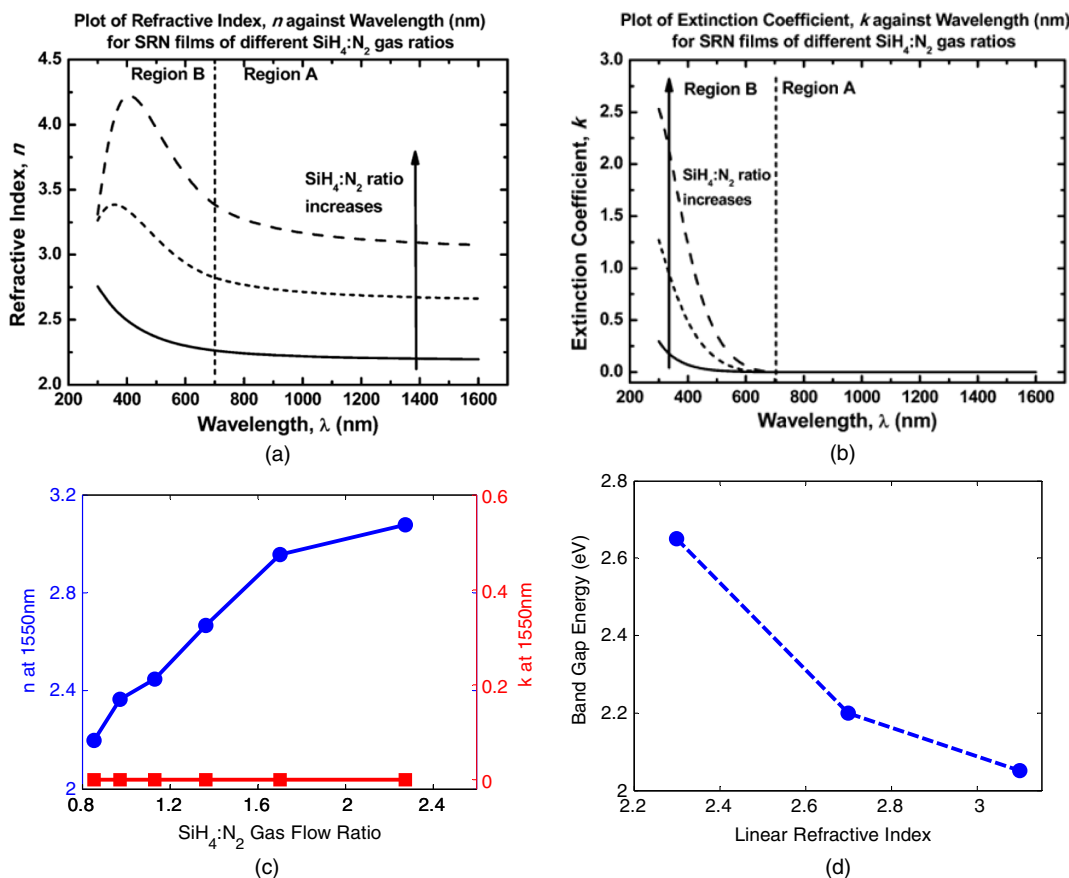


Fig. 1. Tailoring of the refractive index of silicon-rich nitride films grown using low-temperature (250°C) inductively coupled chemical vapor deposition. (a) It is observed that the measured refractive index of films increases as the $\text{SiH}_4:\text{N}_2$ ratio increases from 0.85 to 1.36 to 2.27. (b) The measured extinction coefficient is small beyond 700 nm. At shorter wavelengths, the extinction coefficient becomes larger for higher silicon content. (c) The measured refractive index at 1550 nm as a function of $\text{SiH}_4:\text{N}_2$ process ratio. Varying the $\text{SiH}_4:\text{N}_2$ ratio from the smallest to largest value results in a variation of the refractive index from 2.2 to 3.1. (d) The inverse relation between band gap energy and film refractive index. From Refs. [16,17].

to allow nonlinear refractive indices that are ten times larger than those in stoichiometric silicon nitride [16,18,20]. Substantial efforts to demonstrate tailorability of the silicon-rich nitride films' refractive indices through film composition

have been documented. Trends in the observed film properties indicate that films with higher silicon content generate larger refractive indices, and through the empirical rule availed through Miller, imply a larger nonlinear refractive index as well.

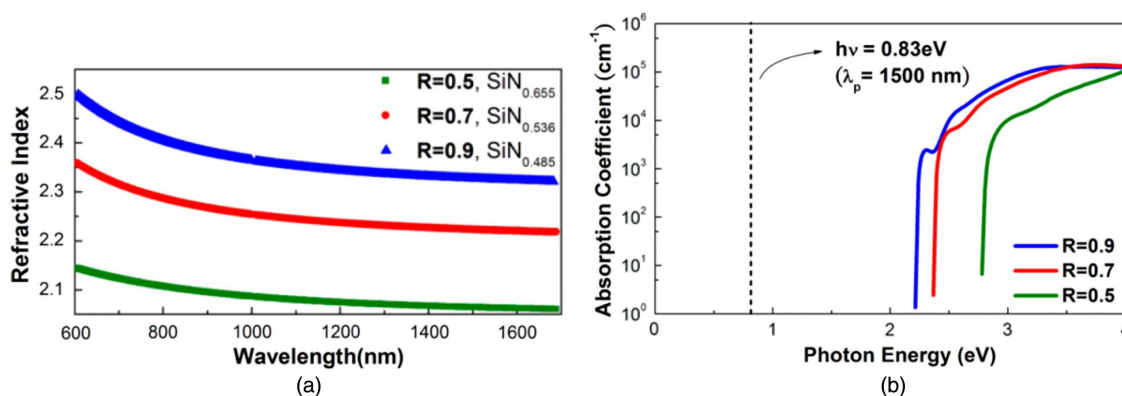


Fig. 2. Refractive index tailoring in plasma-enhanced chemical vapor deposited silicon-rich nitride films. (a) Larger ratios of flow rate between $\text{SiH}_4:\text{NH}_3$ precursor gases result in larger refractive indices. (b) Redshifting of the linear absorption band edge as a function of $\text{SiH}_4:\text{NH}_3$ flow rate ratio. From Ref. [21].

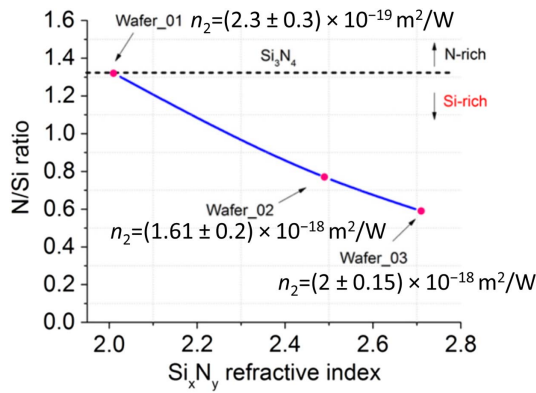


Fig. 3. Refractive index of PECVD-grown silicon-rich nitride films as the N:Si ratio is varied. Films with higher silicon content result in larger refractive indices. From Ref. [28].

Figure 1 documents the variation in the bandgap energy with linear refractive index of ICP-CVD-grown silicon-rich nitride films. As expected from Kramers–Kronig relations and inverse bandgap scaling laws [53], the measured film bandgap decreases as the refractive index increases. A similar phenomenon can be observed in Fig. 2(b), where the absorption spectrum of PECVD-grown SRN films is observed to shift to a lower bandgap energy as the silicon content increases (i.e., refractive index increases).

C. Design Flexibility for Dispersion Engineering

Engineering for anomalous dispersion has now come to be a routine for a large number of nonlinear optics applications, including optical pulse compression [54–58] and supercontinuum generation [17,23,59–61]. Consequently, the ability for a platform to provide flexibility in engineering dispersion of varying signs and magnitude is of great merit. In general, a larger value of Δn (where $\Delta n = n_{\text{core}} - n_{\text{cladding}}$, where n_{core} and n_{cladding} refer to the refractive index of the waveguide core and cladding material, respectively) allows for a greater dynamic range of dispersion engineering to be achieved. The ability to tailor refractive indices anywhere between $n = 2.2$ and $n = 3.1$ is also

an interesting feature that might allow an additional degree of freedom in dispersion engineering of waveguides and optical nanostructures. Indeed, various groups have leveraged tailored waveguide geometries to achieve dispersion profiles that facilitate the nonlinear optical phenomenon under study. Both low-temperature ICP-CVD-grown films [25] and high-temperature LPCVD-grown films [24] have been shown to allow for waveguides to be dispersion-engineered according to the needs of the nonlinear optics applications (Fig. 4). In ICP-CVD-grown ultra-silicon-rich nitride (USRN) films, dispersion engineering was demonstrated through the tailoring of waveguide geometries. Fourth-order dispersion, which is important for parametric processes, particularly when the pump is located very close to the zero-dispersion wavelength, was also demonstrated [25]. In LPCVD-grown silicon-rich nitride films [24], waveguides have been engineered to possess two zero-dispersion wavelengths for the facilitation of supercontinuum generation.

3. NONLINEAR OPTICS APPLICATIONS

The interest in silicon-rich nitride for nonlinear optics is fueled by its potential for larger nonlinear parameters compared to stoichiometric silicon nitride, while maintaining a negligible two-photon coefficient at telecommunications wavelengths. Early work involving the characterization of achievable nonlinear parameters in silicon-rich nitride devices leveraged both temporal and spectral measurements. Spectral measurements involving self-phase modulation experiments in silicon-rich nitride films have previously been used for characterizing the nonlinear refractive index [18]. Films with a linear refractive index of 3.1 were observed to possess a nonlinear refractive index of $2.8 \times 10^{-13} \text{ cm}^2/\text{W}$. Using resonance shifts within ring resonators, Lin *et al.* extract the nonlinear refractive index of silicon-rich nitride films with a linear refractive index of 2.49 to be $1.6 \times 10^{-13} \text{ cm}^2/\text{W}$ [20]. Lower-index films ($n = 2.1$) have been shown to possess a nonlinear refractive index of $6 \times 10^{-15} \text{ cm}^2/\text{W}$ [19]. More recently, PECVD-grown SRN films with a linear refractive index of 2.7 were characterized to possess a nonlinear refractive index of $2.0 \times 10^{-14} \text{ cm}^2/\text{W}$ [28], whereas LPCVD-grown SRN films with

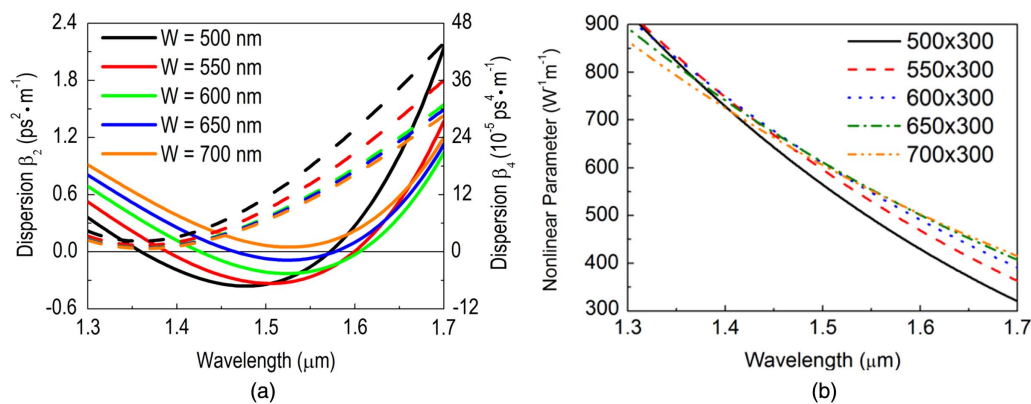


Fig. 4. (a) Calculated second-order (β_2) and fourth-order (β_4) dispersion of ICP-CVD-grown USRN waveguides for different waveguide widths (W) for a fixed height of 300 nm. (b) Calculated nonlinear parameter of the USRN waveguides as a function of wavelength for various waveguide widths (W) and fixed height of 300 nm.

a linear refractive index of 2.2 were shown to possess a nonlinear refractive index of $1.1 \times 10^{-14} \text{ cm}^2/\text{W}$ [43]. Collectively, the data available on the nonlinear refractive index of various silicon-rich nitride films confirm the empirical rule developed by Miller—larger linear refractive indices generate larger nonlinear refractive indices as well.

The benefit of a large linear refractive index to nonlinear optics applications is multi-fold. First, a large core refractive index provides a greater dynamic range of achievable dispersion through dispersion engineering [62], a feature that is instrumental for various nonlinear optical processes. Second, as follows from Miller's rule, a linear refractive index implies a larger nonlinear refractive index. The list of CMOS materials on a refractive scale and their nonlinear refractive indices is shown in Fig. 5(a), showing the increase in nonlinear refractive index with increasing linear refractive index, and further showing the inverse relationship with energy bandgap. Third, the nonlinear parameter of a waveguide γ is a function of its effective mode area A_{eff} according to the expression

$$\gamma = \frac{2\pi n_2}{\lambda A_{\text{eff}}}. \quad (1)$$

A larger linear refractive index also enables tighter modal confinement (smaller A_{eff}), thus augmenting the nonlinear parameter [63]. To illustrate the effect of the linear refractive index on the nonlinear parameter, calculated values of A_{eff} for various SiO_2 cladded CMOS waveguides with their geometry optimized for high modal confinement are shown in Fig. 5(b). At the highest end of the spectrum, confined amorphous silicon waveguides with $n = 3.7$ generate an $A_{\text{eff}} \sim 0.16 \mu\text{m}^2$, whereas stoichiometric silicon nitride waveguides with $n = 2.0$ cast in a confined geometry generate an $A_{\text{eff}} \sim 0.75 \mu\text{m}^2$. A core refractive index that is 85% larger leads to an effective mode area that is ~ 5 times smaller or equivalent and contributes to a potential fivefold greater increase in the nonlinear parameter. Table 1 lists several nonlinear optical applications, which we will discuss in detail.

Table 1. List of Nonlinear Optics Applications

| | |
|----|---|
| 1. | Wavelength Conversion |
| 2. | Optical Parametric Amplification |
| 3. | Supercontinuum Generation |
| 4. | Nonlinear All-Optical Signal Processing |
| 5. | Enhanced Light–Matter Interaction |

A. Wavelength Conversion

One of the most attractive applications of nonlinear optics is the generation of light at new wavelengths. In degenerate four-wave mixing, wavelength conversion follows the expression $\omega_{\text{idler}} = 2 \cdot \omega_{\text{pump}} - \omega_{\text{signal}}$ [63]. Conversion efficiency in parametric processes is also tied to the phase mismatch between the pump, signal, and idler. The maximum conversion efficiency of an idler at any given pump power is achieved when there is phase matching. This is given by $G_{\text{max}} = \sin^2(\gamma \cdot P_{\text{pump}} \cdot L)$ [64]. Therefore, engineering waveguides with the requisite anomalous dispersion and large nonlinear parameters allow for parametric wavelength conversion to be optimized. Engineering for anomalous dispersion has now come to be a routine for a large number of nonlinear optics applications including optical pulse compression [54–58] and supercontinuum generation [17,23,59–61].

In Kerr-based nonlinear optics, four-wave mixing serves as the mechanism for several optical signal processes including optical parametric amplification [49,50,65,66] and frequency comb generation [5,12–15]. Wavelength conversion at telecommunications wavelengths has been explored using continuous wave light, with different formulations of silicon-rich nitride waveguides [17,19,28]. Four-wave mixing experiments performed at 1550 nm using waveguides fabricated from ultra-silicon-rich nitride films with a material composition of Si_7N_3 and a linear refractive index of 3.1 demonstrated a conversion efficiency of -26 dBm using powers of up to 14 dBm [17,25]. Using a pump located at 1535 nm, conversion of a signal

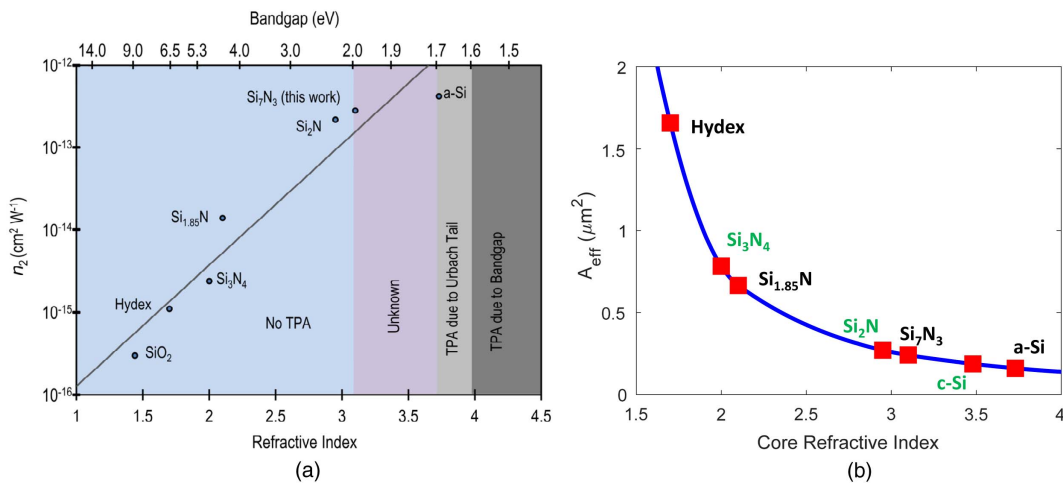


Fig. 5. (a) Amorphous CMOS materials as a function of linear refractive index. Films with larger linear refractive indices possess larger nonlinear refractive indices and smaller bandgaps [6,11,16–21,25,48–52,62,67]. The relationship between bandgap and refractive index is fitted empirically with reported values. From Ref. [25]. (b) Calculated waveguide mode effective areas for various SiO_2 -cladded CMOS waveguides with their geometry optimized for high modal confinement.

located at 1620 nm to an idler located at 1450 nm is demonstrated, representing broadband wavelength conversion over 170 nm [Fig. 6(b)]. In these experiments, the conversion efficiency was not observed to plateau for pump powers of up to 14 dBm, and a log-linear relationship between pump power and conversion efficiency was achieved, confirming the absence of two-photon effects at the wavelength of operation [Fig. 6(c)].

LPCVD-grown SRN waveguides with a linear refractive index of 2.1 demonstrated conversion efficiencies of up to -37 dB using 30 dBm of continuous wave power [19]. In these experiments, plateauing of the conversion efficiency was also not observed. Notably, the high continuous-wave powers used in these experiments did not lead to any reported material degradation or modifications to their optical properties. In amorphous silicon waveguides, which are similar to SRN in their amorphous nature and CMOS compatibility, stable material compositions have been reported [68]. However, several groups have also reported degradation/modifications in their optical properties over time, varying in extent according to the experimental conditions [61,69].

Greater conversion efficiency may also be achieved by increasing the power level of the pump. Pulsed pumps provide peak powers that are many times larger than their average. The peak power of pulses can be extracted using the expression

$$P_{\text{peak}} = \frac{1}{R_p T} \int S(\lambda) d\lambda, \quad (2)$$

where R_p , T , and $S(\lambda)$ represent the repetition rate of the laser, temporal pulse width, and spectral profile of the pulse, respectively. Four-wave mixing experiments were performed using LPCVD-grown SRN waveguides with a linear refractive index of 2.1 and a silicon content of ~55% [23]. A pulsed pump at 1552 nm was combined with a continuous-wave signal at 1562 nm using a fiber optic coupler. A conversion efficiency (CE) of -13.6 dB at a peak pump power of 40.5 dBm was reported [Fig. 7(a)]. In this set of experiments, the conversion efficiency is observed to retain a linear relationship with the input peak power up to the highest pump power of 40.5 dB, signifying negligible nonlinear loss effects [Fig. 7(b)].

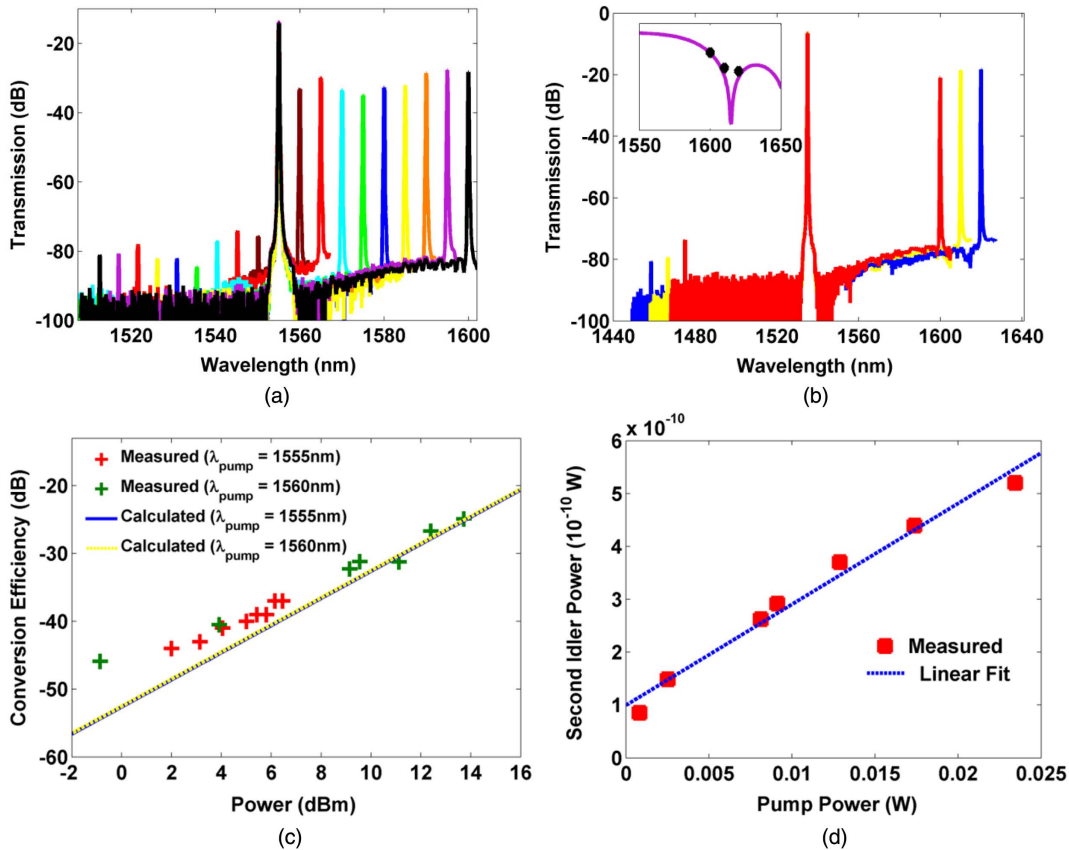


Fig. 6. (a) Generated four-wave-mixing spectra as the signal wavelength is tuned from 1560 to 1610 nm using a pump located at 1555 nm. Brown, red, cyan, green, blue, yellow, orange, purple, and black lines denote the four-wave-mixing spectra for a signal located at 1560, 1565, 1570, 1575, 1580, 1585, 1590, 1595, and 1600 nm, respectively. (b) Four-wave-mixing using a pump at 1535 nm and signal at 1620 nm, representing conversion over 170 nm. Red, yellow, and blue lines denote the four-wave-mixing spectra for a signal located at 1600, 1610, and 1620 nm, respectively. Inset shows the calculated (purple line) and measured (black diamonds) conversion efficiency as a function of wavelength. (c) Measured conversion efficiency as a function of the pump power. Blue solid and yellow dashed lines represent the calculated conversion efficiency as a function of the pump power for a pump wavelength of 1555 nm and 1560 nm, respectively. (d) Four-wave-mixing experiments using a pump at 1560 nm and a signal at 1555 nm. From Refs. [17,25].

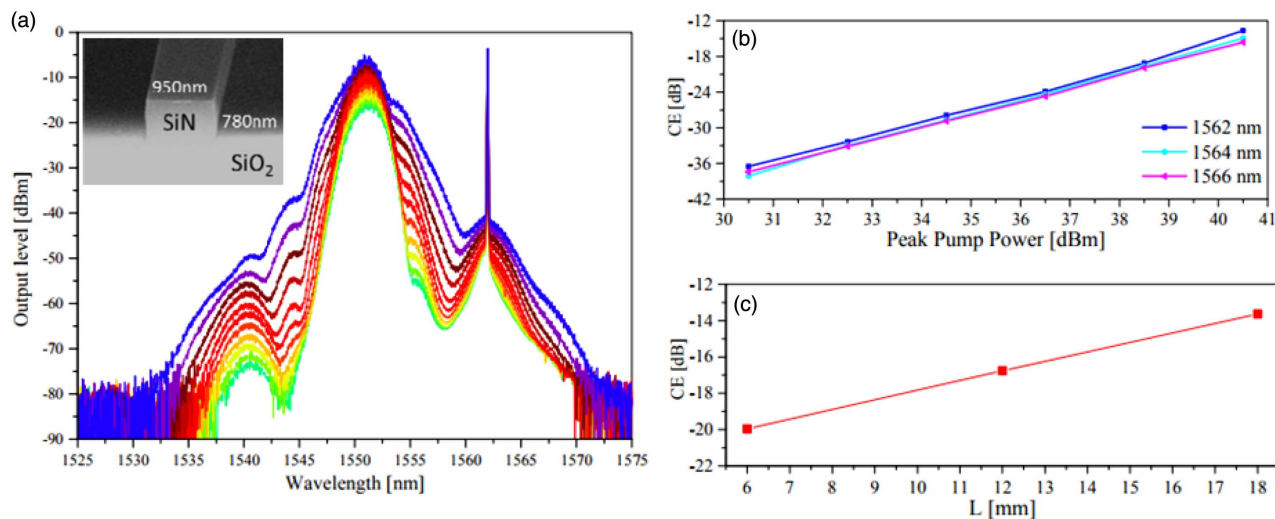


Fig. 7. (a) Four-wave mixing spectra using an LPCVD-grown silicon rich nitride waveguide. The inset shows the scanning electron micrograph of the fabricated waveguide. Conversion efficiency as a function of (b) peak pump power and (c) SRN waveguide length. A peak pump power of 40.5 dBm generates a conversion efficiency of 13.6 dB in a 1.8 cm SRN waveguide. From Ref. [23].

B. Optical Parametric Amplification

Light amplification through parametric processes allows light at targeted wavelengths to be amplified using a high-powered pump. Phase matching provides the mechanism for selecting the wavelengths that get amplified. Optical parametric amplification was previously demonstrated at telecommunications wavelengths in crystalline silicon waveguides [65]. The difficulty of achieving high gain was attributed to the presence of two-photon and free-carrier absorption. The broadband nature of the amplification was achieved by maintaining a low anomalous dispersion across a wide bandwidth. On/off parametric gain of 5.2 dB was achieved, representing the first demonstration of optical parametric gain on a CMOS chip. Since then, optical parametric gain based on several CMOS platforms has been achieved [49,50,70]. Amorphous silicon waveguides with a nonlinear parameter of $770 \text{ W}^{-1}/\text{m}$ and a non-zero two-photon absorption coefficient have also been used to demonstrate optical parametric gain of 26.5 dB [49]. The significantly larger gain compared to that demonstrated in crystalline silicon may be attributed to the larger nonlinear figure of merit in a-Si compared to crystalline silicon (~ 2.1 versus ~ 0.5), as well as the larger nonlinear parameter. It is worth noting that the platforms where higher parametric gain was demonstrated possessed higher nonlinear figures of merit, but not necessarily a larger nonlinearity. In Hydrex glass for example, large optical parametric gain of up to 16.5 dB was demonstrated using waveguides with a nonlinear parameter of $0.22 \text{ W}^{-1}/\text{m}$ and a zero two-photon absorption coefficient [70]. This represents a gain that is more than 10 dB larger than that in crystalline silicon optical parametric amplifiers at the $1.55 \text{ }\mu\text{m}$ wavelength, even though the nonlinear parameter is three orders of magnitude smaller. As further testimony to the criticality of the nonlinear figure of merit, silicon waveguides have been used for high-gain optical parametric amplification of up to 30 dB, albeit at wavelengths beyond $2.2 \text{ }\mu\text{m}$ where the two-photon absorption coefficient becomes zero

and three-photon absorption becomes the dominant nonlinear absorption mechanism [71]. The nonlinear figure of merit for crystalline silicon has previously been measured to have a peak value of ~ 4 at a wavelength of $2.2 \text{ }\mu\text{m}$, as expected from two-photon resonance [66]. Thus, despite the large nonlinear parameter magnitude of silicon waveguides, we see that the nonlinear losses have a large detrimental effect on the efficiency of the parametric process.

USRN waveguides, which are dispersion engineered to be weakly anomalous across a wide bandwidth while retaining a large nonlinear parameter, have recently been used to realize high-gain optical parametric amplification at telecommunications wavelengths. Using films with a linear refractive index of 3.1, 7 mm long waveguides with a nonlinear parameter of $\sim 500 \text{ W}^{-1}/\text{m}$ and two zero-dispersion wavelengths at $\sim 1.4 \text{ }\mu\text{m}$ and $\sim 1.6 \text{ }\mu\text{m}$ were used to demonstrate optical parametric amplification. A 500 fs pulsed pump located at 1555 nm was combined with a continuous-wave signal beyond 1620 nm using a wavelength division multiplexer. Using a peak power of 14 W, signal gains of up to 42.5 dB were demonstrated, as well as cascaded four-wave mixing down to the third idler. The gain in the first, second, and third idlers was 36.2, 21.2, and 7.7 dB, respectively. Figure 8 shows the four-wave mixing spectra achieved using the USRN waveguides, which together with the cascaded four-wave mixing effect extends the optical spectrum from 1300 nm to beyond 1700 nm (OSA limited). In a similar vein, the observation of optical parametric amplification in crystalline silicon waveguides in the region of negligible two-photon absorption beyond $2.2 \text{ }\mu\text{m}$ was accompanied with cascaded four-wave mixing as well [71].

In silicon-based nonlinear optics, it has been documented that free-carrier-induced reductions in nonlinear efficiency become more severe when the temporal pulse width becomes longer. At one end of the spectrum lies continuous-wave excitation, which incurs significant free-carrier buildup at intensities of $\sim 50 \text{ MW}/\text{cm}^2$ [3]. Ultrashort pulses have been

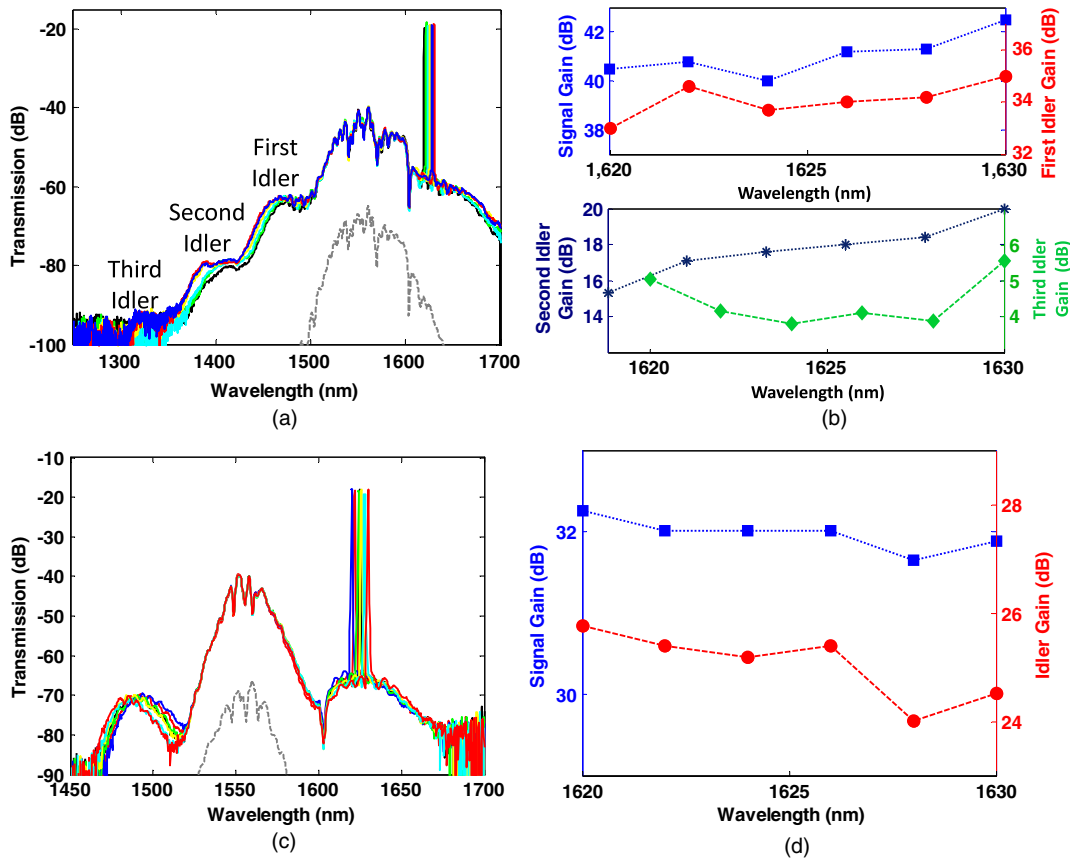


Fig. 8. (a) Four-wave mixing spectra as a function of wavelength for a peak pump power of 14 W using USRN waveguides. Cascaded four-wave-mixing is observed, including second and third idlers, which extend the spectrum to 1300 nm. Black, green, cyan, yellow, blue, and red lines represent measured spectra with the signal wavelength at 1620, 1622, 1624, 1626, 1628, and 1630 nm, respectively. The grey dashed curve represents the pump spectrum offset by -25 dB, with the signal off. (b) Measured parametric gain in the signal (blue squares), first (red circles), second (dark blue stars), and third idlers (green diamonds). (c) Transmission spectrum as a function of wavelength for a peak pump power of 10 W. Blue, orange, green, yellow, cyan, and red lines denote measured spectra with the signal wavelength at 1620, 1622, 1624, 1626, 1628, and 1630 nm, respectively. Grey dashed curve denotes the pump spectrum offset by -25 dB, with the signal off. (d) Measured signal (blue squares) and idler gain (red circles) as a function of signal wavelength. From Ref. [25].

documented to induce less severe free-carrier-induced penalties in silicon-on-insulator waveguides [4,72–74]. In optical parametric amplification experiments using USRN waveguides, the achievable parametric gain when using a pump with the same peak power with different temporal widths was studied. Using a peak power of 10 W, similar parametric gain was achieved using a 500 fs pump and 2 ps pump at 32.3 dB and 30 dB, respectively. This result confirms the negligible nonlinear losses in the USRN device at the 1550 nm wavelength.

C. Supercontinuum Generation

Similar to parametric wavelength conversion, the generation of a broadband supercontinuum relies on the Kerr nonlinearity and appropriately engineered waveguide dispersion. Launching the pump close to the zero-dispersion wavelength of the waveguide catalyzes a rich multitude of nonlinear processes, including cascaded four-wave mixing, Cerenkov radiation, and dispersive wave generation. These processes cause the generated supercontinuum to be much wider than that from pure self-phase modulation (SPM) effects [75,76].

SPM as a solitary effect allows for spectral broadening, but to a limited extent. The injection of optical pulses with high peak powers into appropriately designed waveguides does not necessarily evolve into a supercontinuum if the waveguides are sufficiently short to preclude higher-order effects such as cascaded four-wave mixing or soliton fission. Nevertheless, the ability for silicon-rich nitride waveguides to support high peak powers without nonlinear losses allows for extended spectral broadening from the singular self-phase modulation effect within short waveguide lengths. USRN waveguides were used to investigate the ability of the waveguides to withstand high powers without degradation or nonlinear losses, while preserving wideband spectral broadening. Using waveguides as short as 430 μm , a doubling of the input pulse spectrum at the -30 dB level can be achieved, and using waveguides as short as 1.6 mm, close to 5x broadening of the input pulse spectrum is achieved with a peak power of 66 W [Fig. 9(a)] [22]. Consistent with pulse propagation calculations using the nonlinear Schrödinger equation for a TPA-free medium, the spectral bandwidth grows linearly with power [Figs. 9(c) and 9(d)]. Normalizing to the

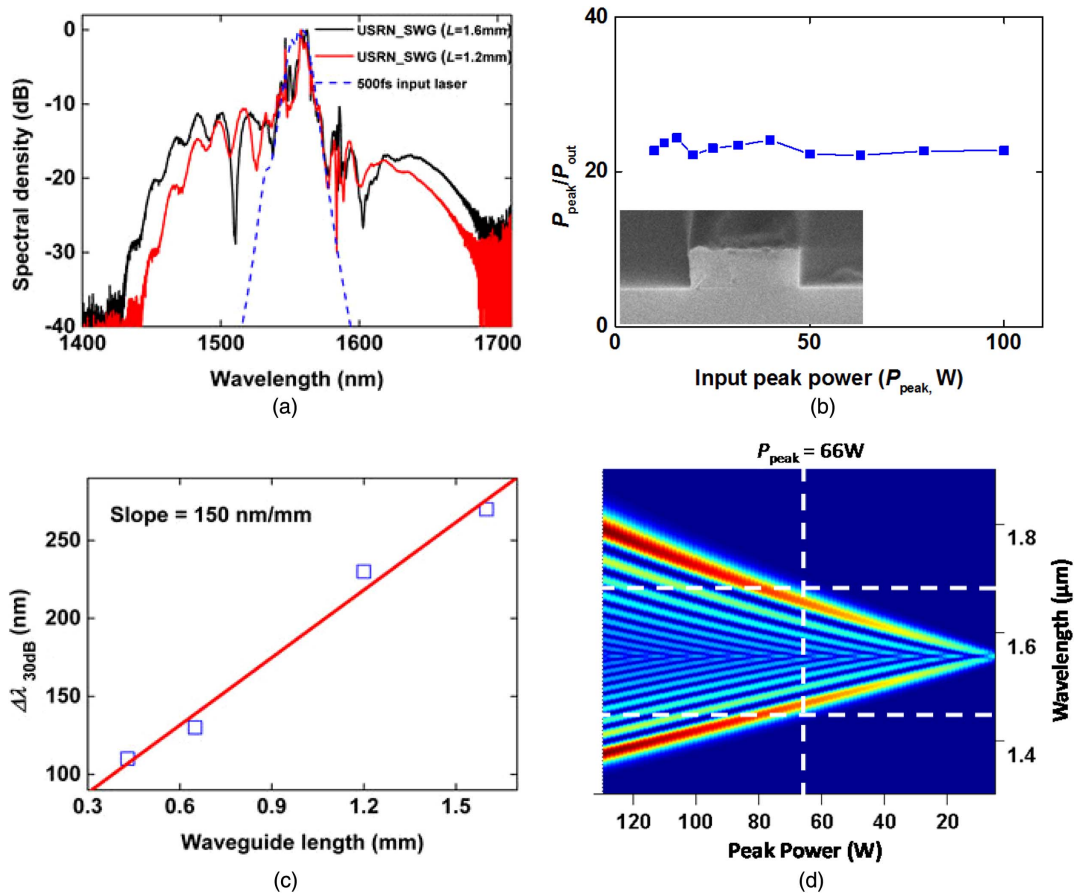


Fig. 9. (a) Output spectra of 1.2 mm (red solid line) and 1.6 mm (black solid line) USRN waveguides compared with femtosecond laser spectrum (blue dashed line). Seed pulses are 500 fs wide with a peak power of 66 W. (b) Measured value of $P_{\text{peak}}/P_{\text{out}}$ versus P_{peak} . That the flat profile obtained for $P_{\text{peak}}/P_{\text{out}}$ as P_{peak} is varied implies negligible nonlinear losses. (c) Spectral bandwidth at the -30 dB level as a function of waveguide length. (d) Simulated evolution of the 500 fs pulses as a function of the input peak power. From Ref. [22].

waveguide length, a figure of merit that measures the degree of spectral broadening per unit length [$F_b = \Delta\lambda_{\text{out}}/(\Delta\lambda_{\text{in}} \cdot L)$, mm^{-1}], is adopted. A figure of merit of 3.2 mm^{-1} is achieved. To place this in context with other CMOS platforms, silicon-on-insulator waveguides and amorphous silicon waveguides possess the next highest values of F_b . Crystalline silicon waveguides that possess nonlinear parameters of similar magnitude to the USRN waveguides demonstrate broadening factors of $\sim 0.9 \text{ mm}^{-1}$, and amorphous silicon waveguides that possess somewhat larger nonlinear parameters than USRN waveguides have demonstrated broadening factors of $\sim 1.7 \text{ mm}^{-1}$. A flat profile for $P_{\text{peak}}/P_{\text{out}}$ versus P_{peak} is observed [Fig. 8(b)], as well as a linear increase in the -30 dB bandwidth of the pulse as a function of the USRN waveguide length [Fig. 8(c)], consistent with the minimal nonlinear losses in the waveguides. Again, the ability for the USRN platform to leverage ultralarge nonlinear parameters without degradation in photonic quantum efficiencies from nonlinear losses can be assessed through the spectral broadening efficiencies observed in ultrashort USRN waveguides.

The leveraging of ultrashort USRN waveguides for large spectral broadening remains solidly in the SPM regime. Pulses do not propagate through a sufficiently long waveguide

to stimulate observable initiation of secondary nonlinear effects such as dispersive wave formation, soliton fission, or cascaded four-wave mixing. To verify the presence of secondary nonlinear optical effects in longer USRN waveguides, 500 fs pulses at 1555 nm were launched into anomalously dispersive waveguides with a length of 6 mm. The waveguides are characterized using SPM experiments to possess a nonlinear parameter of $550 \text{ W}^{-1}/\text{m}$ [18]. At power levels varying between 3 and 140 W, output spectra of USRN waveguides were observed to evolve into a wideband supercontinuum (Fig. 10). The onset of dispersive wave formation is clearly observed at an input peak power of 75 W. The location of the dispersive wave relative to the input peak power allowed the third-order dispersion to be extracted as $35 \text{ ps}^3/\text{km}$ [Fig. 10(c)]. A peak power of 140 W generates a supercontinuum that extends to $1.13 \mu\text{m}$ on the blue side of the spectrum and beyond $1.75 \mu\text{m}$ (OSA limited) on the red side of the spectrum (Fig. 10).

In LPCVD-grown silicon-rich nitride waveguides, a supercontinuum spanning an octave has been demonstrated [24]. The waveguides are reported to possess a nonlinearity of $5.7 \text{ W}^{-1}/\text{m}$, and no two-photon absorption at telecommunications wavelengths. Using 130 fs seed pulses at a peak power of 760 W, a wideband supercontinuum spanning from

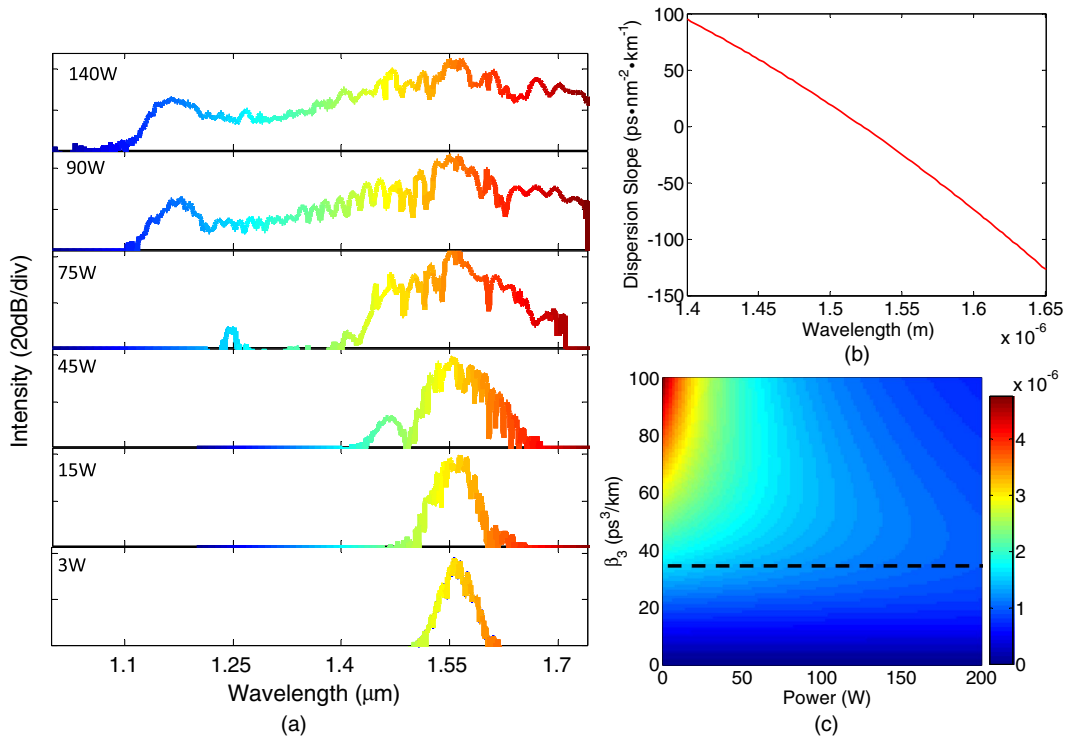


Fig. 10. Characterization of supercontinuum from the SRN waveguide. (a) Spectral output as a function of input peak power. The location of the dispersive wave varies as a function of input peak power. (b) Dispersion slope calculated from the waveguide's second-order dispersion. (c) Theoretical location of the generated dispersive wave as a function of third-order dispersion and input peak power. The color bar represents the wavelength of the dispersive wave corresponding to each color in the plot. The value of $\beta_3 = 35 \text{ ps}^3/\text{km}$ provides the best agreement with the locations of the dispersive waves generated in the experiment. From Ref. [18].

800 to 2400 nm at the -30 dB level is achieved with 10 mm long waveguides (Fig. 11). The efficiency of the supercontinuum is facilitated by the presence of two zero-dispersion wavelengths, between which dispersion for the quasi-transverse-electric (TE) mode in the waveguide is anomalous and small in magnitude [Fig. 11(a)], as well as the formation of dispersive waves on both the red and blue sides of the generated spectrum located beyond $2.2 \mu\text{m}$ and below 850 nm , respectively.

The results are impressive, especially when juxtaposed with silicon-based supercontinuum experiments, which are much more limited in comparison [59,77]. Again, the importance of TPA-free operation for nonlinear applications is evident.

D. Nonlinear All-Optical Signal Processing

Various nonlinear experiments within the temporal and spectral domains have been performed using silicon-rich nitride

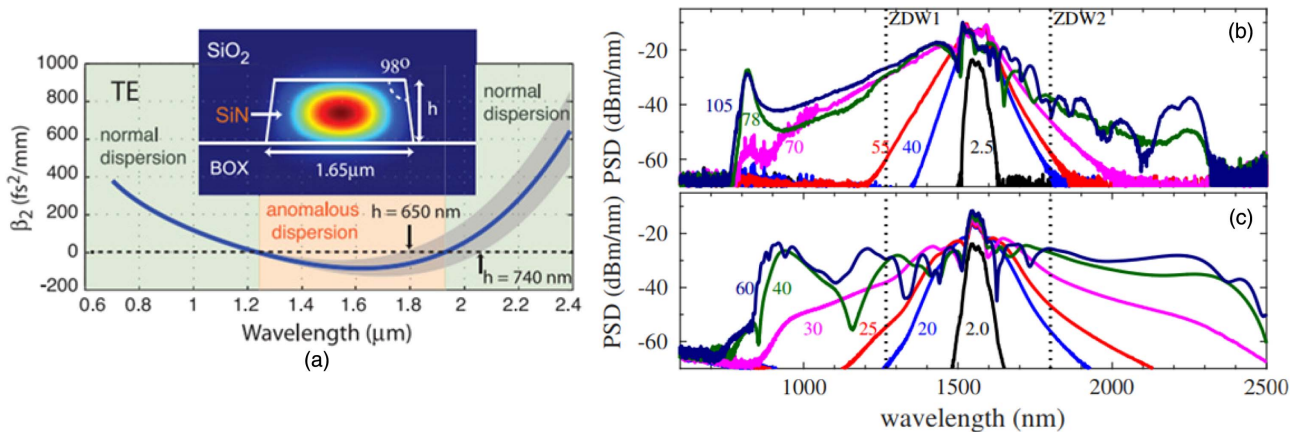


Fig. 11. (a) Calculated group velocity dispersion of an LPCVD-grown silicon-rich nitride waveguide with two zero-dispersion wavelengths (ZDWs). (b) Experimental and (c) calculated supercontinuum spectra using pulses with a temporal width of 130 fs. The power spectral density at the waveguide's output is averaged over 50 noise realizations. From Ref. [23].

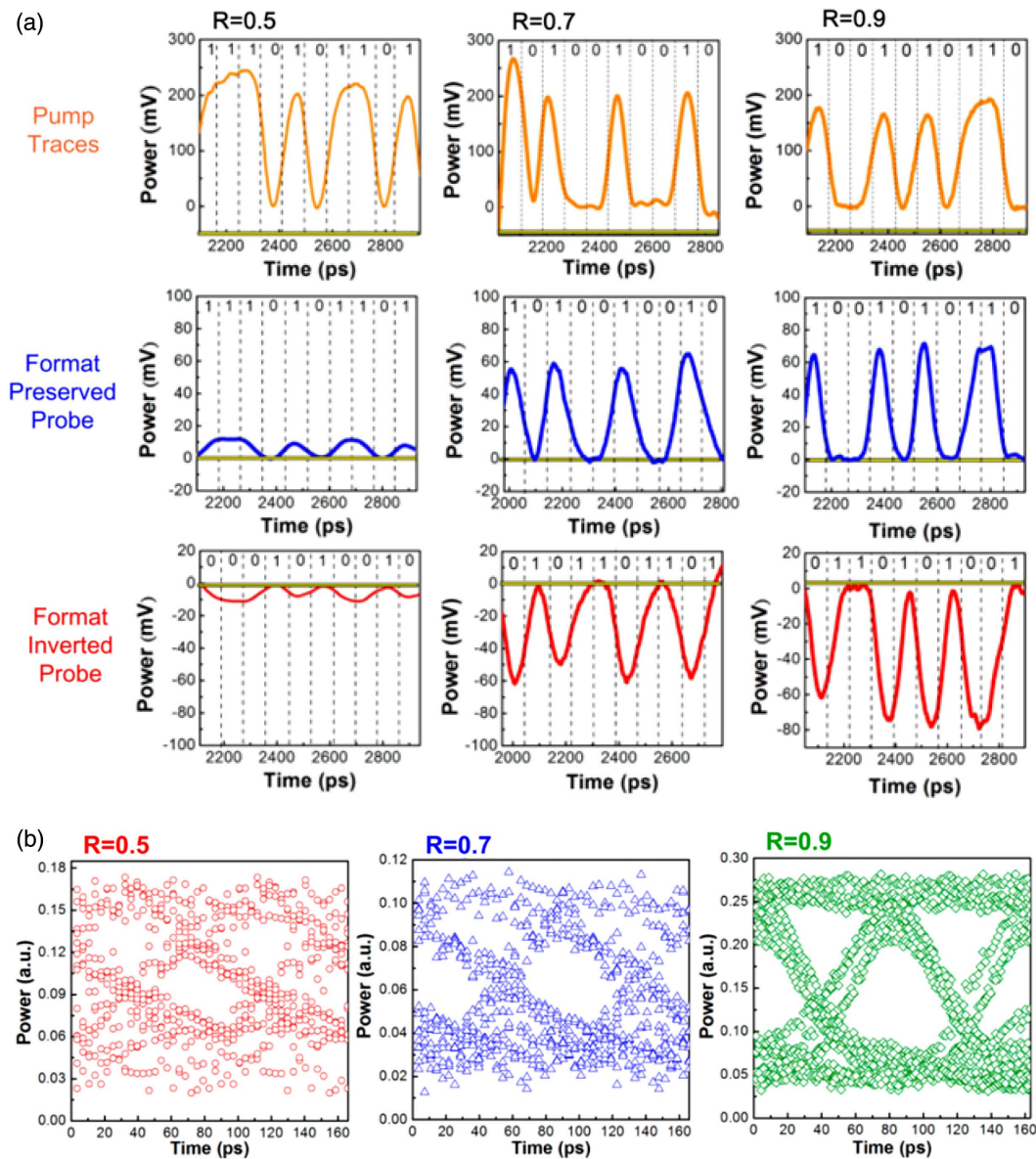


Fig. 12. (a) Top row shows the 12 Gbit/s pulsed RZ-OOK data encoded within the pump and injected into three Si-rich Si_xN_{4-x} microring resonators with varying Si content. $R = 0.9$ represents the Si-rich Si_xN_{4-x} microring resonator with the highest Si content. The middle row shows the probe signal that has been modulated with the data from the pump after experiencing the Kerr nonlinearity in the Si-rich Si_xN_{4-x} microring resonators. The lower row shows the probe signal that has been modulated with inverted data from the pump. Modulation contrast is greatest for $R = 0.9$. (b) Measured eye diagrams for the three ring resonators. The Si-rich Si_xN_{4-x} microring resonator with the largest Si content ($R = 0.9$) has the highest modulation contrast and most open eye. From Ref. [20].

photonic waveguides. In 2015, the processing of signals using the Kerr effect in SRN waveguides with a linear and nonlinear refractive index of 2.49 and $1.6 \times 10^{-13} \text{ cm}^2/\text{W}$, respectively, was demonstrated for data conversion and inversion of 12 Gbit/s pulsed return-to-zero, on-off keying (RZ-OOK) data [20]. Leveraging microring resonators fabricated from the Si-rich Si_xN_{4-x} films, a pump located near 1550 nm is tuned to a resonance of the resonator. A probe signal for which the data from the pump is to be encoded is tuned to a separate resonance of the microring resonator. When the pump is on, shifts in the resonance wavelengths occur as a result of the Kerr-induced increase in the effective refractive index, $\Delta n = n_2 I M$, where

I is the intensity of the pump and M is the intensity enhancement factor from the ring resonator. The 12 Gbit/s pulsed RZ-OOK data was encoded into the pump using a Mach-Zehnder modulator, and the resulting signals with the modulated and inverted data formats are shown in Fig. 12(a). It was observed that the demonstrated modulation contrast and openness of the eye diagrams increase with nonlinear refractive index (or Si content). The results demonstrate the importance of the nonlinear refractive index in the efficiency of nonlinear optical signal processing. Importantly, the characterization of the rise and fall times of the converted signals reveals a value of 29 ps, a value that is very similar to that of the pump data

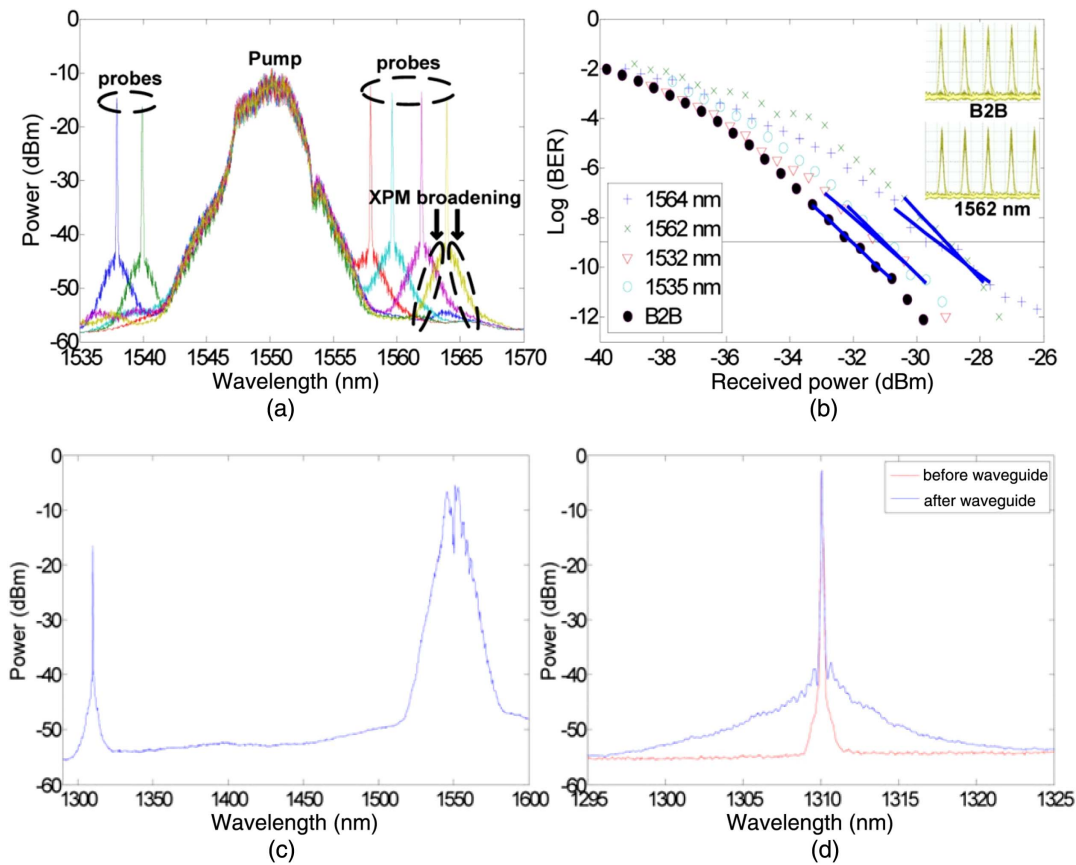


Fig. 13. (a) Wavelength conversion of 10 Gb/s signals for various probe wavelengths using LPCVD-grown silicon-rich nitride waveguides. (b) Measured bit error rate (BER) as a function of received power. Inset shows the electrical eye diagrams for the data signal (back-to-back) as well as the wavelength converted signal at 1562 nm for error-free operation (50 ps/div). (c) XPM-based spectral broadening of a probe at 1310 nm using a pump located at 1550 nm. (d) Close up of the XPM-broadened probe at 1310 nm. From Ref. [29].

stream, implying that there are minimal transient delays. Conversely in silicon-based all-optical switches [38,78], free-carrier limitations in the temporal response have been shown to range between hundreds of picoseconds and the order of nanoseconds. Consequently, TPA-free operation of the Si-rich SiN_x data processor provides a significant advantage in speed over their silicon-based counterparts.

More recently, waveguides fabricated from LPCVD-grown SRN films with a linear and nonlinear refractive index of 2.1 and $1.4 \times 10^{-18} \text{ m}^2/\text{W}$, respectively, were used for wavelength conversion of 10 Gb/s signals across the C-band [29]. A Mach-Zehnder modulator was used to encode 10 Gb/s RZ-OOK data into a continuous-wave pump with 33 dBm of power before it was combined with a continuous-wave signal (Fig. 12). Cross-phase modulation of the co-propagating signal and data-encoded pump results in the generation of sidebands around the signal and encoding of the data onto the signal. Bit-error-rate characterization of the converted data shows that a bit error rate $<10^{-9}$ is achieved for various converted signal wavelengths with power penalties between 1.6 dB and 3.4 dB. Importantly, the presence of nonlinear losses was not observed in these SRN waveguides for peak powers of up to 55 W. Cross-phase modulation (XPM)-based spectral broadening was also observed using a probe at 1310 nm and a 10 GHz

pulse train as the pump, implying a wavelength difference between pump and probe of 240 nm [Figs. 13(c) and 13(d)].

E. Enhanced Light-Matter Interaction

The ability to augment nonlinear effects in integrated optical devices is highly desired to reduce requisite power levels for observation of nonlinear phenomena and reduction of device footprint. Further, certain advanced nonlinear effects are not possible through nanowire waveguides, for example, because of the large differences between the nonlinear lengths and dispersive lengths. In nanowire waveguides, even with intentional dispersion engineering, group velocity dispersions no larger than the order of $1000 \text{ ps}\cdot\text{nm}^{-1}\cdot\text{km}^{-1}$ are realizable. When juxtaposed with the resulting nonlinear parameters (few to hundreds of W^{-1}/m), nonlinear lengths in nanowire waveguides are often much shorter than dispersive lengths, particularly when the peak power levels are a few hundred milliwatts or higher. Solitons, for example, would benefit from having dispersion lengths and nonlinear lengths that are similar in magnitude [55,57,79]. For the observation of nonlinear phenomena, which relies strongly on dispersive effects such as optical pulse compression [54,56], nanostructures with much larger engineered dispersion would be required. When this

Table 2. Nonlinear Optical Properties for Various CMOS Platforms^a

| | c-Si | a-Si | Hydex | Si ₃ N ₄ | Si _{1.85} N | Si _{1.25} N | Si ₂ N | Si ₇ N ₃ |
|--|-----------------------|-----------------------|------------------------|--------------------------------|------------------------|------------------------|------------------------|--------------------------------|
| n_2 (cm ² /W) | 4.5×10^{-13} | 2.1×10^{-13} | 1.10×10^{-15} | 2.40×10^{-15} | 1.40×10^{-14} | 1.60×10^{-14} | 1.60×10^{-13} | 2.80×10^{-13} |
| γ (W ⁻¹ /m) | 300 | 1200 | 0.25 | 0.65 | 6.1 | 16 | 206 | 430–550 |
| β_{TPA} (cm · GW ⁻¹) | 0.45 | 0.25 | nil | nil | nil | nil | nil | nil |
| FOM _{NL} | 0.86 | 5 | $\gg 1$ | $\gg 1$ | $\gg 1$ | $\gg 1$ | $\gg 1$ | $\gg 1$ |
| Propagation Loss (dB/cm) | ~ 1 | ~ 4.5 | 0.06 | 8×10^{-4} | ~ 1 | 1.5 | ~ 1 | 1.9–4.5 |
| $\gamma \cdot L_{\text{eff,max}}$ (W ⁻¹) | N/A | N/A | 0.18 | 3.5 | 0.27 | 0.46 | 8.9 | 4.8–9.8 |
| Thermal Budget | N/A | Low | Low | High | High | Low | Low | Low |
| Reference | [53] | [68] | [5,6] | [14] | [19] | [28] | [21] | [25] |

^aLow thermal budget refers to deposition temperatures <400°C, compatibility with back-end CMOS processing.

is not possible to implement on photonic waveguides with limited dispersion, engineered dispersive elements have been used to provide the requisite dispersion [27,77,80,81].

Photonic crystal waveguides possess engineered bandgaps that arise from a periodic lattice. Similar to the emergence of a material bandgap arising from the periodicity of the atomic arrangement, the periodicity in refractive index within a two-dimensional plane creates a photonic bandgap. Within the photonic bandgap, dispersion becomes significant at the band edge. Further, creating a region of flat and large group indices close to the band edge can augment $\chi^{(3)}$ nonlinear effects by a factor S^2 , given by the expression [82,83]

$$S^2 = \left(\frac{n_g}{n_0} \right)^2. \quad (3)$$

While an appropriately designed photonic crystal allows for significant enhancements in nonlinear optical effects, nonlinear losses, if present, would also be augmented by the same factor. Materials possessing two-photon absorption at the application wavelength would acquire an effective two-photon absorption coefficient,

$$\beta_{\text{TPA,eff}} = \frac{\beta_{\text{TPA,bulk}}}{A_{\text{eff}}} S^2. \quad (4)$$

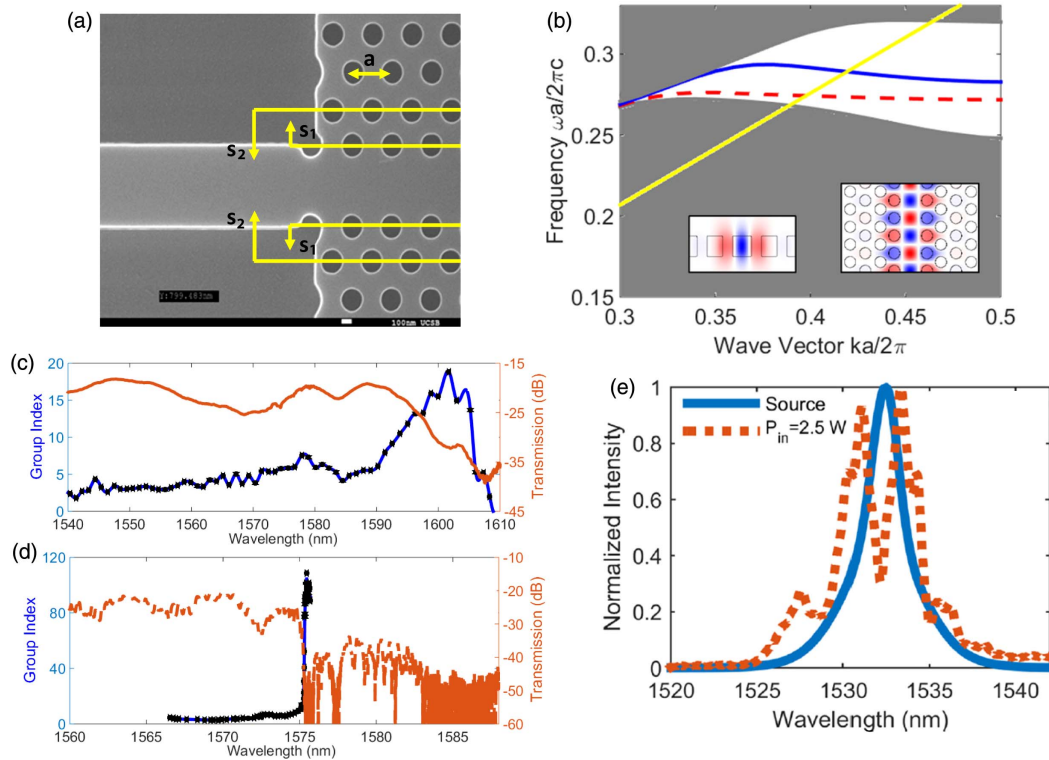


Fig. 14. Ultra-silicon-rich nitride photonic crystal waveguide (PhCWs). (a) Scanning electron micrograph of a USRN photonic crystal waveguide. s_1 and s_2 denote the direction of hole shifts to engineer a region of flat group index near the band edge; r denotes the radius of the PhCW holes. (b) Calculated and diagram for PhCW with $r = 135$ nm, $s_1 = 30$ nm, and $s_2 = 0$, insets show the mode profiles from the propagation direction and the top of PhCW, red dashed graph corresponds to the band of interest. Light line for SiO₂ cladding is shown in yellow. (c) Measured transmission (red solid line) and group index (black squares) of a flat-band dispersion-engineered USRN PhCW. (d) Measured transmission (red dashed line) and group index (black squares) of a non-flat-band dispersion-engineered USRN PhCW. (e) Measured source spectrum (blue solid line) and output spectrum of a 96.6 μm PhCW (red dashed line) at a peak power of 2.5 W. A 1.5π nonlinear phase shift is acquired by the input pulse. From Ref. [27].

Consequently, any enhancement in nonlinear optical effects from operating at a flat-band slow light region with a high group index also results in stronger nonlinear losses. This is indeed the case for the crystalline silicon platform, where the vast majority of work in nonlinear CMOS photonic crystals has been implemented. The desire to ameliorate nonlinear loss mechanisms has led to other high-index materials with larger nonlinear figures of merit being used to demonstrate nonlinear phenomena in photonic crystal waveguides. These include InGaAP [55], chalcogenides such as Ag-As₂Se₃ [84], and Ge₃₃As₁₂Se₅₅ [85], which although not CMOS compatible, allow for efficient nonlinear phase acquisition. Very large effective nonlinearities that are on the order of $10^4 \text{ W}^{-1}/\text{m}$ have been demonstrated in these platforms through slow light enhancements.

The implementation of photonic crystal waveguides using silicon-rich nitride films would likewise allow for a fortuitous combination of S^2 scaling in the effective nonlinear parameter, while ensuring that the nonlinear losses are minimal and CMOS compatibility is maintained. W1 and W0.7 photonic crystal waveguides have recently been implemented on silicon-rich

nitride films with a linear refractive index of 2.54 [47]. The achievable group index is as high as 110 on the band edge, and variable transmission bandwidths are demonstrated in the W1 and W0.7 designs (Fig. 13). As expected through the group index scaling, propagation losses increase with the group index.

Meanwhile, flat-band engineering of USRN photonic crystal waveguides has been used to create a region of relatively constant group index [27]. The lateral shifts of the two rows of holes parallel to the direction of field propagation are adopted to flatten the group index profile close to the band edge. Using this technique, a flat band group index of ~ 19 over a bandwidth of 5 nm was designed [Fig. 14(b)]. In similar USRN photonic crystal waveguides without flat-band engineering, group indices as high as 108 were achieved, though expectedly at the cost of reduced bandwidth [Fig. 15(c)].

Within the flat-band region, self-phase modulation experiments using 1.9 ps pulses at a 20 MHz repetition rate were performed in 96.6 μm long USRN photonic crystal waveguides. A nonlinear phase of 1.5π was acquired at a peak power of 2.5 W. This allows for an effective nonlinear parameter of $1.97 \times 10^4 \text{ W}^{-1} \cdot \text{m}^{-1}$ to be extracted, similar in magnitude to

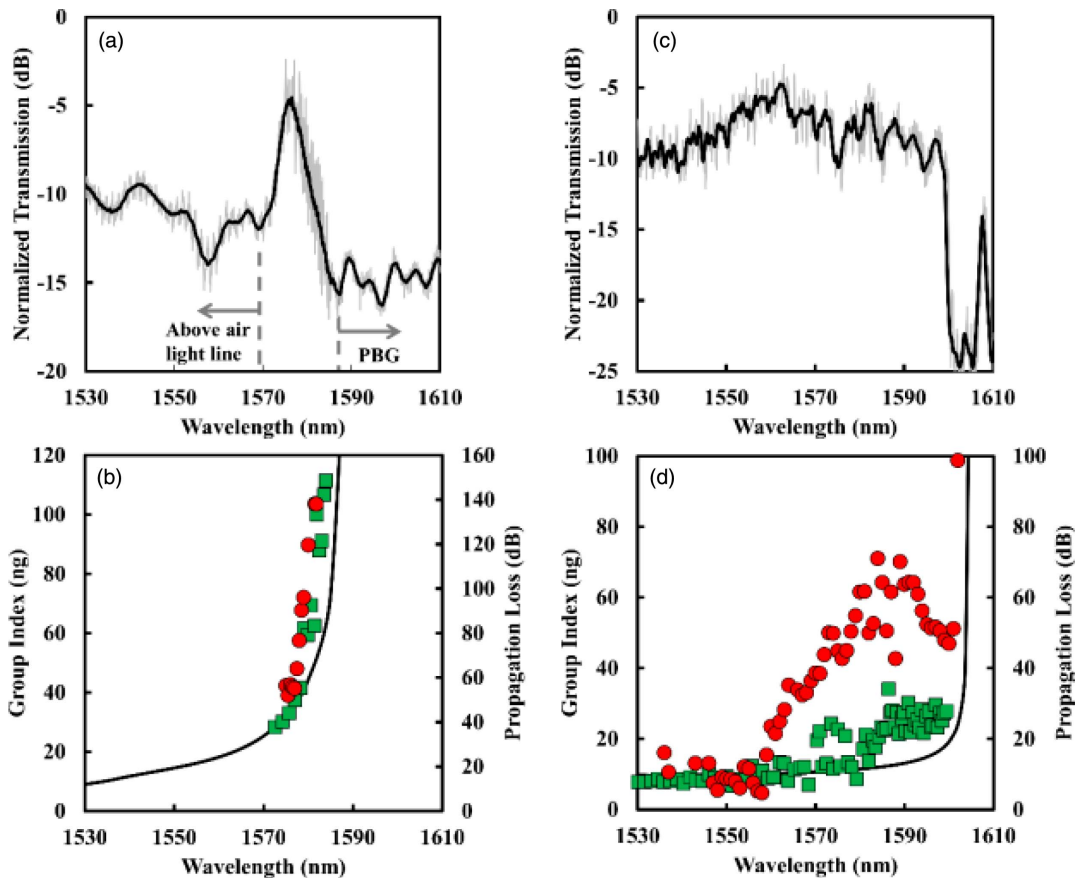


Fig. 15. (a) Gray and black curves show the measured transmission spectrum of a W1 photonic crystal waveguide with a length of 200 μm and a lattice period of 580 nm. The transmission region is about 20 nm and highlighted by the dashed lines. (b) Calculated (black solid line) and estimated (green squares) group index values of the fabricated showing the highest estimated group index of 110. The waveguide propagation loss is denoted by red dots, and the lowest propagation loss measured was 53 dB/cm for a group index of 37. (c) Gray and black curves show the measured transmission spectrum with a transmission bandwidth of over 70 nm for a W0.7 photonic crystal waveguide with a length of 200 μm and a lattice period of 580 nm. (d) Calculated (black solid line) and estimated (green squares) group index values of the fabricated. The highest estimated group index is 34. The waveguide propagation loss is denoted by red dots, and the lowest measured propagation loss was 4.6 dB/cm for a group index of 7.4. From Ref. [47].

that achievable in chalcogenide and crystalline silicon photonic crystal waveguides while eliminating the detrimental effects of two-photon or free-carrier losses. Though still in its early stages, these USRN waveguides show promise for lower powers and smaller device footprints required to observe nonlinear optical effects.

4. OUTLOOK AND OPPORTUNITIES

Thus far, nonlinear optics using silicon-rich nitride devices has shown their ability to generate nonlinear parameters anywhere between 5x to 500x larger than those in stoichiometric silicon nitride devices, while maintaining the high nonlinear figure of merit. The maximum achievable nonlinear phase, $\phi_{\text{NL,max}}$, acquired by an optical field with a peak power P_{peak} is given by the expression $\phi_{\text{NL,max}} = \gamma \cdot P_{\text{peak}} \cdot L_{\text{eff,max}}$, where the maximum effective length of the waveguide $L_{\text{eff,max}} = 1/\alpha$, and α is the loss coefficient of the waveguide [63]. In Table 2, we compare the nonlinear optical properties for various CMOS platforms. When comparing some of the results with other CMOS platforms, silicon-rich nitride's potential for lower power operation or devices with smaller footprints appears promising. Recent results in silicon nitride suggest that propagation losses as low as 0.8 dB/m are achievable and place the threshold for optical parametric oscillation well below 1 mW [14]. In high FOM_{NL} platforms, P_{peak} is not attenuated by nonlinear losses, and the ability for a platform to efficiently acquire nonlinear phase can be assessed through the figure of merit, $\gamma \cdot L_{\text{eff,max}}$ (W⁻¹) [25], where $L_{\text{eff,max}}$ represents the maximum effective length of the waveguide and is given by $1/\alpha$, and α is the loss coefficient of the waveguide. Stoichiometric silicon nitride waveguides in Ref. [14] possess a $\gamma \cdot L_{\text{eff,max}}$ value of 3.5, whereas silicon-rich nitrides have been demonstrated to possess a $\gamma \cdot L_{\text{eff,max}}$ value of close to 10 [21,25]. These figures of merit highlight the strong potential for silicon-rich nitride for waveguide-based broadband nonlinear optics applications.

One potential opportunity in the field of SRN-based nonlinear optics involves resonator-enhanced nonlinear optics. The use of resonators limits the bandwidth of optical signals that can be processed, but greatly lowers the powers needed to observe nonlinear effects. Serving as the basis for frequency combs and low-power Kerr-based switching, resonator-enhanced nonlinear optics has seen extensive progress in high nonlinear figure of merit CMOS platforms including Hydex [5,85–88], Si₃N₄ [12–15,88–91], and crystalline silicon at mid-infrared wavelengths [92,93]. Nonlinear effects in resonators follow different scaling laws compared to purely waveguide-based devices—nonlinear phase from a resonator scales with the square of the resonator finesse [25,94]. In ultralow-loss Si₃N₄, resonators with finesse as high as $\sim 4 \times 10^4$ are achievable [14]. Today's SRN resonators are nowhere close to these finesse values, and efforts towards process enhancements are needed to place them on par with other ultralow-loss CMOS platforms. Finally, the time is ripe for silicon-rich nitride nonlinear devices to expand their applicability towards the fields of microwave photonics and quantum information science. Both fields benefit from platforms with advantageous nonlinear properties and good nonlinear figures of merit, and more work

needs to be done to study the use of SRN devices towards each field.

5. CONCLUSIONS

We have reviewed recent progress in nonlinear optics leveraging silicon-rich nitride devices. It is still in its nascent stages compared to the amount of progress that has been made in other CMOS nonlinear platforms such as crystalline silicon, amorphous silicon, Hydex glass, and stoichiometric silicon nitride. However, recent developments show that silicon-rich-nitride-based nonlinear optics is highly promising as an alternative platform providing a high nonlinear figure of merit at telecommunications wavelengths and large nonlinear parameters as much as 500x larger than those in stoichiometric silicon nitride waveguides. In addition, their compatibility with CMOS processing allows them to be seamlessly integrated with electronics. Further innovations in device design and advanced optical systems will establish silicon-rich-nitride-based integrated photonic devices as a mainstay in on-chip nonlinear optical signal processing, perhaps enabling new phenomena not previously observable in other CMOS platforms.

Funding. MOE Academic Research Fund Tier 2 Grant, National Research Foundation Competitive Research Grant, National Research Foundation Land and Liveability National Innovation Challenge Grant, SUTD-MIT International Design Center, and Temasek Laboratories grant; National Research Foundation, Prime Minister's Office, Singapore, under its Medium Sized Centre Program.

REFERENCES

1. A. Mekis, S. Abdalla, D. Foltz, S. Gloeckner, S. Hovey, S. Jackson, Y. Liang, M. Mack, G. Masini, M. Peterson, T. Pinguet, S. Sahni, M. Sharp, P. Sun, D. Tan, L. Verslegers, B. P. Welch, K. Yokoyama, S. Yu, and P. M. de Dobbelaere, "A CMOS photonics platform for high-speed optical interconnects," in *IEEE Photonics Conference* (IEEE, 2012), pp. 356–357.
2. R. C. Miller, "Optical second harmonic generation in piezoelectric crystals," *Appl. Phys. Lett.* **5**, 17–19 (1964).
3. E. Dulkeith, Y. A. Vlasov, X. Chen, N. C. Panoiu, and R. M. Osgood, "Self-phase-modulation in submicron silicon-on-insulator photonic wires," *Opt. Express* **14**, 5524–5534 (2006).
4. I. W. Hsieh, X. Chen, J. I. Dadap, N. C. Panoiu, R. M. Osgood, S. J. McNab, and Y. A. Vlasov, "Ultrafast-pulse self-phase modulation and third-order dispersion in Si photonic wire-waveguides," *Opt. Express* **14**, 12380–12387 (2006).
5. L. Razzari, D. Duchesne, M. Ferrera, R. Morandotti, S. Chu, B. E. Little, and D. J. Moss, "CMOS-compatible integrated optical hyper-parametric oscillator," *Nat. Photonics* **4**, 41–45 (2010).
6. M. Ferrera, L. Razzari, D. Duchesne, R. Morandotti, Z. Yang, M. Liscidini, J. E. Sipe, S. Chu, B. E. Little, and D. J. Moss, "Low-power continuous-wave nonlinear optics in doped silica glass integrated waveguide structure," *Nat. Photonics* **2**, 737–740 (2008).
7. D. Duchesne, M. Ferrera, L. Razzari, R. Morandotti, B. E. Little, S. T. Chu, and D. J. Moss, "Efficient self-phase modulation in low loss, high index doped silica glass integrated waveguides," *Opt. Express* **17**, 1865–1870 (2009).
8. A. Pasquazi, M. Peccianti, Y. Park, B. E. Little, S. T. Chu, R. Morandotti, J. Azana, and D. J. Moss, "Sub-picosecond phase-sensitive optical pulse characterization on a chip," *Nat. Photonics* **5**, 618–623 (2011).
9. D. J. Moss, R. Morandotti, A. L. Gaeta, and M. Lipson, "New CMOS-compatible platforms based on silicon nitride and Hydex for nonlinear optics," *Nat. Photonics* **7**, 597–607 (2013).

10. K. Ikeda, R. E. Saperstein, N. Alic, and Y. Fainman, "Thermal and Kerr nonlinear properties of plasma-deposited silicon nitride/silicon dioxide waveguides," *Opt. Express* **16**, 12987–12994 (2008).
11. D. T. H. Tan, K. Ikeda, P. C. Sun, and Y. Fainman, "Group velocity dispersion and self phase modulation in silicon nitride waveguides," *Appl. Phys. Lett.* **96**, 061101 (2010).
12. J. S. Levy, A. Gondarenko, M. A. Foster, A. C. Turner-Foster, A. L. Gaeta, and M. Lipson, "CMOS-compatible multiple-wavelength oscillator for on-chip optical interconnects," *Nat. Photonics* **4**, 37–40 (2010).
13. Y. Okawachi, K. Saha, J. S. Levy, Y. H. Wen, M. Lipson, and A. L. Gaeta, "Octave-spanning frequency comb generation in a silicon nitride chip," *Opt. Lett.* **36**, 3398–3400 (2011).
14. X. Ji, F. A. S. Barbosa, S. P. Roberts, A. Dutt, J. Cardenas, Y. Okawachi, A. Bryant, A. L. Gaeta, and M. Lipson, "Ultra-low-loss on-chip resonators with sub-milliwatt parametric oscillation threshold," *Optica* **4**, 619–624 (2017).
15. P. Marin-Palomo, J. N. Kemal, M. Karpov, A. Kordts, J. Pfeifle, M. H. P. Pfeiffer, P. Trocha, S. Wolf, V. Brasch, M. H. Anderson, R. Rosenberger, K. Vijayan, W. Freude, T. J. Kippenberg, and C. Koos, "Microresonator-based solitons for massively parallel coherent optical communications," *Nature* **546**, 274–279 (2017).
16. D. K. T. Ng, Q. Wang, T. Wang, S. K. Ng, Y. T. Toh, K. P. Lim, Y. Yang, and D. T. H. Tan, "Exploring high refractive index silicon-rich nitride films by low temperature inductively coupled plasma chemical vapor deposition and applications for integrated waveguides," *ACS Appl. Mater. Interfaces* **7**, 21884–21889 (2015).
17. K. J. A. Ooi, D. K. T. Ng, T. Wang, A. K. L. Chee, L. K. Ang, Q. Wang, and D. T. H. Tan, "Ultralow power, broadband continuous wave four wave mixing in silicon rich nitride waveguides," in *Nonlinear Optics*, OSA Technical Digest Series (Optical Society of America, 2015), paper NTh3A.9.
18. T. Wang, D. K. T. Ng, S. K. Ng, Y. T. Toh, A. K. L. Chee, G. F. R. Chen, Q. Wang, and D. T. H. Tan, "Supercontinuum generation in bandgap engineered, back-end CMOS compatible silicon rich nitride waveguides," *Laser Photon. Rev.* **9**, 498–506 (2015).
19. C. J. Krückel, A. Fülöp, T. Klüntberg, J. Bengtsson, P. A. Andrekson, and V. Torres-Company, "Linear and nonlinear characterization of low-stress high-confinement silicon-rich nitride waveguides," *Opt. Express* **23**, 25827–25837 (2015).
20. G. R. Lin, S. P. Su, C. L. Wu, Y. H. Lin, B. J. Huang, H. Y. Wang, C. T. Tsai, C. I. Wu, and Y. C. Chi, "Si-rich SiN_x based Kerr switch enables optical data conversion up to 12 Gbit/s," *Sci. Rep.* **5**, 9611 (2015).
21. C. L. Wu, Y. H. Lin, S. P. Su, B. J. Huang, C. T. Tsai, H. Y. Wang, Y. C. Chi, C. I. Wu, and G. R. Lin, "Enhancing optical nonlinearity in a nonstoichiometric SiN waveguide for cross-wavelength all-optical data processing," *ACS Photon.* **2**, 1141–1154 (2015).
22. J. W. Choi, G. F. R. Chen, D. K. T. Ng, K. J. A. Ooi, and D. T. H. Tan, "Wideband nonlinear spectral broadening in ultra-short ultra-silicon rich nitride waveguides," *Sci. Rep.* **6**, 27120 (2016).
23. M. Mitrovic, X. Guan, H. Ji, L. K. Oxenløwe, and L. H. Frandsen, "Four-wave mixing in silicon-rich nitride waveguides," in *Frontiers in Optics*, OSA Technical Digest Series (Optical Society of America, 2015), paper FM1D.6.
24. X. Liu, M. Pu, B. Zhou, C. J. Krückel, A. Fülöp, V. Torres-Company, and M. Bache, "Octave-spanning supercontinuum generation in a silicon-rich nitride waveguide," *Opt. Lett.* **41**, 2719–2722 (2016).
25. K. J. A. Ooi, D. K. T. Ng, T. Wang, A. K. L. Chee, S. K. Ng, Q. Wang, L. K. Ang, A. M. Agarwal, L. C. Kimerling, and D. T. H. Tan, "Pushing the limits of CMOS optical parametric amplifiers with USRN:Si₃N₄ above the two-photon absorption edge," *Nat. Commun.* **8**, 13878 (2017).
26. P. Xing, G. F. R. Chen, X. Zhao, M. C. Tan, and D. T. H. Tan, "Silicon rich nitride ring resonators for rare-earth doped C-band amplifiers pumped at the O-band," *Sci. Rep.* **7**, 9101 (2017).
27. E. Sahin, K. J. A. Ooi, G. F. R. Chen, D. K. T. Ng, C. E. Png, and D. T. H. Tan, "Enhanced optical nonlinearities in CMOS-compatible ultra-silicon-rich nitride photonic crystal waveguides," *Appl. Phys. Lett.* **110**, 161113 (2017).
28. C. Lacava, S. Stankovic, A. Z. Khokhar, T. D. Bucio, F. Y. Gardes, G. T. Reed, D. J. Richardson, and P. Petropoulos, "Si-rich silicon nitride for nonlinear signal processing applications," *Sci. Rep.* **7**, 22 (2017).
29. M. R. Dizaji, C. J. Krückel, A. Fülöp, P. A. Andrekson, V. Torres-Company, and L. R. Chen, "Silicon-rich nitride waveguides for ultra-broadband nonlinear signal processing," *Opt. Express* **25**, 12100–12108 (2017).
30. L. Dal Negro, J. H. Yi, L. C. Kimerling, S. Hamel, A. Williamson, and G. Gallí, "Light emission from silicon-rich nitride nanostructures," *Appl. Phys. Lett.* **88**, 183103 (2006).
31. L. Dal Negro, J. H. Yi, J. Michel, L. C. Kimerling, T.-W. F. Chang, V. Sukhovatkin, and E. H. Sargent, "Light emission efficiency and dynamics in silicon-rich silicon nitride films," *Appl. Phys. Lett.* **88**, 233109 (2006).
32. H. Mertens, K. N. Andersen, and W. E. Svendsen, "Optical loss analysis of silicon rich nitride waveguides," in *European Conference on Optical Communications* (IEEE, 2002), paper p1.38.
33. T. Barwicz, "Silicon photonics for energy-efficient interconnects," *J. Opt. Netw.* **6**, 63–72 (2007).
34. F. Urbach, "The long-wavelength edge of photographic sensitivity and of the electronic absorption of solids," *Phys. Rev.* **92**, 1324 (1953).
35. I. Goykhman, B. Desiatov, and U. Levy, "Ultrathin silicon nitride micro-ring resonator for bio-photonic applications at 970 nm wavelength," *Appl. Phys. Lett.* **97**, 081108 (2010).
36. M. Tien, J. F. Bauters, M. J. R. Heck, D. J. Blumenthal, and J. E. Bowers, "Ultra-low loss Si₃N₄ waveguides with low nonlinearity and high power handling capability," *Opt. Express* **18**, 23562–23568 (2010).
37. A. Subramanian, P. Neutens, A. Dhakal, R. Jansen, T. Claes, X. Rottenberg, F. Peyskens, S. Selvaraja, P. Helin, B. Dubois, K. Leyssens, S. Severi, P. Deshpande, R. Baets, and P. Van Dorpe, "Low-loss single mode PECVD silicon nitride photonic wire waveguides for 532–900 nm wavelength window fabricated within a CMOS pilot line," *IEEE Photon. J.* **5**, 2202809 (2013).
38. C. Boehme and G. Lucovsky, "Dissociation reactions of hydrogen in remote plasma-enhanced chemical vapor-deposition silicon nitride," *J. Vac. Sci. Technol. A* **19**, 2622–2628 (2001).
39. H. T. Philipp, K. N. Andersen, W. Svendsen, and H. Ou, "Amorphous silicon rich silicon nitride optical waveguides for high density integrated optics," *Electron Lett.* **40**, 419–421 (2004).
40. S. C. Mao, S. H. Tao, Y. L. Xu, X. W. Sun, M. B. Yu, G. Q. Lo, and D. L. Kwong, "Low propagation loss SiN optical waveguide prepared by optimal low-hydrogen module," *Opt. Express* **16**, 20809–20816 (2008).
41. F. Ay and A. Aydinli, "Comparative investigation of hydrogen bonding in silicon based PECVD grown dielectrics for optical waveguides," *Opt. Mater.* **26**, 33–46 (2004).
42. A. Gondarenko, J. S. Levy, and M. Lipson, "High confinement micron-scale silicon nitride high Q ring resonator," *Opt. Express* **17**, 11366–11370 (2009).
43. C. J. Krückel, A. Fülöp, Z. Ye, P. A. Andrekson, and V. Torres-Company, "Optical bandgap engineering in nonlinear silicon nitride waveguides," *Opt. Express* **25**, 15370–15380 (2017).
44. F. L. Martinez, A. del Prado, I. Martil, G. Gonzalez-Diaz, W. Böhne, W. Fuhs, J. Rohrich, B. Selle, and I. Sieber, "Molecular models and activation energies for bonding rearrangement in plasma-deposited a-SiN_x:H dielectric thin films treated by rapid thermal annealing," *Phys. Rev. B* **63**, 245320 (2001).
45. K. N. Andersen, W. E. Svendsen, T. Stimpel-Lindner, T. Sulima, and H. Baumgartner, "Annealing and deposition effects of the chemical composition of silicon-rich nitride," *Appl. Surf. Sci.* **243**, 401–408 (2005).
46. V. R. Almeida, C. A. Barrios, R. R. Panepucci, M. Lipson, M. A. Foster, D. G. Ouzounov, and A. L. Gaeta, "All-optical switching on a silicon chip," *Opt. Lett.* **29**, 2867–2869 (2004).
47. K. Debnath, T. D. Bucio, A. Al-Attili, A. Z. Khokhar, S. Saito, and F. Y. Gardes, "Photonic crystal waveguides on silicon rich nitride platform," *Opt. Express* **25**, 3214–3221 (2017).
48. Y. Shoji, T. Ogasawara, T. Kamei, Y. Sakakibara, S. Suda, K. Kintaka, H. Kawashima, M. Okano, T. Hasama, H. Ishikawa, and M. Mori, "Ultrafast nonlinear effects in hydrogenated amorphous silicon wire waveguides," *Opt. Express* **18**, 5668–5673 (2010).
49. B. Kuyken, S. Clemmen, S. K. Selvaraja, W. Bogaerts, D. Van Thourhout, P. Emplit, S. Massar, G. Roelkens, and R. Baets, "On-chip parametric amplification with 26.5 dB gain at telecommunication wavelengths using CMOS-compatible hydrogenated amorphous silicon waveguides," *Opt. Lett.* **36**, 552–554 (2011).

50. K. Y. Wang and A. C. Foster, "GHz-rate optical parametric amplifier in hydrogenated amorphous silicon," *J. Opt.* **17**, 094012 (2015).
51. K. Narayanan and S. F. Preble, "Optical nonlinearities in hydrogenated-amorphous silicon waveguides," *Opt. Express* **18**, 8998–9005 (2010).
52. K. Y. Wang and A. C. Foster, "Ultralow power continuous-wave frequency conversion in hydrogenated amorphous silicon waveguides," *Opt. Lett.* **37**, 1331–1333 (2012).
53. V. Lucarini, J. J. Saarinen, K. E. Peiponen, and E. M. Vartiainen, *Kramers-Kronig Relations in Optical Materials Research* (Springer, 2005).
54. D. T. H. Tan, P. C. Sun, and Y. Fainman, "Monolithic nonlinear pulse compressor on a silicon chip," *Nat. Commun.* **1**, 116 (2010).
55. P. Colman, C. Husko, S. Combr  , I. Sagnes, C. W. Wong, and A. De Rossi, "Temporal solitons and pulse compression in photonic crystal waveguides," *Nat. Photonics* **4**, 862–868 (2010).
56. D. T. H. Tan, "Optical pulse compression on a silicon chip: effect of group velocity dispersion and free carriers," *Appl. Phys. Lett.* **101**, 211112 (2012).
57. A. Blanco-Redondo, C. Husko, D. Eades, Y. Zhang, J. Li, T. F. Krauss, and B. J. Eggleton, "Observation of soliton compression in silicon photonic crystals," *Nat. Commun.* **5**, 3160 (2014).
58. D. T. H. Tan, A. M. Agarwal, and L. C. Kimerling, "Nonlinear photonic waveguides for on-chip optical pulse compression," *Laser Photon. Rev.* **9**, 294–308 (2015).
59. I. W. Hsieh, X. Chen, X. Liu, J. I. Dadap, N. C. Panoiu, C. Y. Chou, F. Xia, W. M. Green, Y. A. Vlasov, and R. M. Osgood, "Supercontinuum generation in silicon photonic wires," *Opt. Express* **15**, 15242–15248 (2007).
60. R. Halir, Y. Okawachi, J. S. Levy, M. A. Foster, M. Lipson, and A. L. Gaeta, "Ultrabroadband supercontinuum generation in a CMOS-compatible platform," *Opt. Lett.* **37**, 1685–1687 (2012).
61. J. Safioui, F. Leo, B. Kuyken, S.-P. Gorza, S. K. Selvaraja, R. Baets, Ph. Emplit, G. Roelkens, and S. Massar, "Supercontinuum generation in hydrogenated amorphous silicon waveguides at telecommunication wavelengths," *Opt. Express* **22**, 3089–3097 (2014).
62. A. C. Turner, C. Manolatou, B. S. Schmidt, M. Lipson, M. A. Foster, J. E. Sharping, and A. L. Gaeta, "Tailored anomalous group-velocity dispersion in silicon channel waveguides," *Opt. Express* **14**, 4357–4362 (2006).
63. Q. Lin, O. J. Painter, and G. P. Agrawal, "Nonlinear optical phenomena in silicon waveguides: modeling and applications," *Opt. Express* **15**, 16604–16644 (2007).
64. G. P. Agrawal, *Nonlinear Fiber Optics*, 2nd ed. (Academic, 1995).
65. M. A. Foster, A. C. Turner, R. Salem, M. Lipson, and A. L. Gaeta, "Broad-band continuous-wave parametric wavelength conversion in silicon nanowaveguides," *Opt. Express* **15**, 12949–12958 (2007).
66. M. A. Foster, A. C. Turner, J. E. Sharping, B. S. Schmidt, M. Lipson, and A. L. Gaeta, "Broad-band optical parametric gain on a silicon photonic chip," *Nature* **441**, 960–963 (2006).
67. C. Grillet, L. Carletti, C. Monat, P. Grosse, B. B. Bakir, S. Menezo, J. M. Fedeli, and D. J. Moss, "Amorphous silicon nanowires combining high nonlinearity, FOM and optical stability," *Opt. Express* **20**, 22609–22615 (2012).
68. T. Wang, N. Venkatram, J. Goscinia  , Y. Cui, G. Qian, W. Ji, and D. T. H. Tan, "Multi-photon absorption and third-order nonlinearity in silicon at mid-infrared wavelengths," *Opt. Express* **21**, 32192–32198 (2013).
69. B. Kuyken, H. Ji, S. Clemmen, S. K. Selvaraja, H. Hu, M. Pu, M. Galili, P. Jeppesen, G. Morthier, S. Massar, L. K. Oxenl  we, G. Roelkens, and R. Baets, "Nonlinear properties of and nonlinear processing in hydrogenated amorphous silicon waveguides," *Opt. Express* **19**, B146–B153 (2011).
70. A. Pasquazi, Y. Park, J. Aza  a, F. L  gar  , R. Morandotti, B. E. Little, S. T. Chu, and D. J. Moss, "Efficient wavelength conversion and net parametric gain via four wave mixing in a high index doped silica waveguide," *Opt. Express* **18**, 7634–7641 (2010).
71. X. Liu, R. M. Osgood, Y. A. Vlasov, and W. M. J. Green, "Mid-infrared optical parametric amplifier using silicon nanophotonic waveguides," *Nat. Photonics* **4**, 557–560 (2010).
72. R. Dekker, A. Driessen, T. Wahlbrink, C. Moormann, J. Niehusmann, and M. F  rst, "Ultrafast Kerr-induced all-optical wavelength conversion in silicon waveguides using 1.55 μm femtosecond pulses," *Opt. Express* **14**, 8336–8346 (2006).
73. L. Yin and G. P. Agrawal, "Impact of two-photon absorption on self-phase modulation in silicon waveguides," *Opt. Lett.* **32**, 2031–2033 (2007).
74. N. Suzuki, "FDTD analysis of two-photon absorption and free-carrier absorption in Si high-index-contrast waveguides," *J. Lightwave Technol.* **25**, 2495–2501 (2007).
75. J. M. Dudley and J. R. Taylor, *Supercontinuum Generation in Optical Fibers* (Cambridge University, 2010).
76. L. Yin, Q. Lin, and G. P. Agrawal, "Soliton fission and supercontinuum generation in silicon waveguides," *Opt. Lett.* **32**, 391–393 (2007).
77. D. T. H. Tan, K. Ikeda, R. E. Saperstein, B. Slutsky, and Y. Fainman, "Chip-scale dispersion engineering using chirped vertical gratings," *Opt. Lett.* **33**, 3013–3015 (2008).
78. D. Dimitropoulos, R. Jhaveri, R. Claps, J. C. S. Woo, and B. Jalali, "Lifetime of photogenerated carriers in silicon-on-insulator rib waveguides," *Appl. Phys. Lett.* **86**, 071115 (2005).
79. J. T. Mok, C. M. de Sterke, I. C. M. Littler, and B. J. Eggleton, "Dispersionless slow light using gap solitons," *Nat. Phys.* **2**, 775–780 (2006).
80. D. T. H. Tan, K. Ikeda, and Y. Fainman, "Coupled chirped vertical gratings for on-chip group velocity dispersion engineering," *Appl. Phys. Lett.* **95**, 141109 (2009).
81. G. F. R. Chen, T. Wang, C. Donnelly, and D. T. H. Tan, "Second and third order dispersion generation using nonlinearly chirped silicon waveguide gratings," *Opt. Express* **21**, 29223–29230 (2013).
82. M. Soljacic, S. G. Johnson, S. Fan, M. Ibanescu, E. Ippen, and J. D. Joannopoulos, "Photonic-crystal slow-light enhancement of nonlinear phase sensitivity," *J. Opt. Soc. Am. B* **19**, 2052–2059 (2002).
83. J. Li, T. P. White, L. O'Faolain, A. Gomez-Iglesias, and T. F. Krauss, "Systematic design of flat band slow light in photonic crystal waveguides," *Opt. Express* **16**, 6227–6232 (2008).
84. K. Suzuki, Y. Hamachi, and T. Baba, "Fabrication and characterization of chalcogenide glass photonic crystal waveguides," *Opt. Express* **17**, 22393–22400 (2009).
85. M. Spurny, L. O'Faolain, D. A. P. Bulla, B. Luther-Davies, and T. F. Krauss, "Fabrication of low loss dispersion engineered chalcogenide photonic crystals," *Opt. Express* **19**, 1991–1996 (2011).
86. M. Peccianti, A. Pasquazi, Y. Park, B. E. Little, S. T. Chu, D. J. Moss, and R. Morandotti, "Demonstration of a stable ultrafast laser based on a nonlinear microcavity," *Nat. Commun.* **3**, 765 (2012).
87. L. Caspani, C. Xiong, B. J. Eggleton, D. Bajoni, M. Liscidini, M. Galli, R. Morandotti, and D. J. Moss, "Integrated sources of photon quantum states based on nonlinear optics," *Light Sci. Appl.* **6**, e17100 (2017).
88. M. Kues, C. Reimer, P. Roztock  , L. R. Cort  s, S. Sciara, B. Wetzell, Y. Zhang, A. Cino, S. T. Chu, B. E. Little, D. J. Moss, L. Caspani, J. Aza  a, and R. Morandotti, "On-chip generation of high-dimensional entangled quantum states and their coherent control," *Nature* **546**, 622–626 (2017).
89. F. Ferdous, H. Miao, D. E. Leaird, K. Srinivasan, J. Wang, L. Chen, L. T. Varghese, and A. M. Weiner, "Spectral line-by-line pulse shaping of on-chip microresonator frequency combs," *Nat. Photonics* **5**, 770–776 (2011).
90. T. J. Kippenberg, R. Holzwarth, and S. A. Diddams, "Microresonator-based optical frequency combs," *Science* **332**, 555–559 (2011).
91. S. W. Huang, H. Zhou, J. Yang, J. F. McMillan, A. Matsko, M. Yu, D. L. Kwong, L. Maleki, and C. W. Wong, "A broadband chip-scale optical frequency synthesizer at 2.7×10^{-16} relative uncertainty," *Phys. Rev. Lett.* **114**, 053901 (2015).
92. B. Kuyken, T. Ideguchi, S. Holzner, M. Yan, T. W. Hansch, J. Van Campenhout, P. Verheyen, S. Coen, F. Leo, R. Baets, G. Roelkens, and N. Picque, "An octave-spanning mid-infrared frequency comb generated in a silicon nanophotonic wire waveguide," *Nat. Commun.* **6**, 6310 (2015).
93. A. G. Griffith, M. Yu, Y. Okawachi, J. Cardenas, A. Mohanty, A. L. Gaeta, and M. Lipson, "Coherent mid-infrared frequency combs in silicon-microresonators in the presence of Raman effects," *Opt. Express* **24**, 13044–13050 (2016).
94. J. E. Heebner and R. W. Boyd, "Enhanced all-optical switching by use of a nonlinear fiber ring resonator," *Opt. Lett.* **24**, 847–849 (1999).